ANNUAL REPORT OF NASA CONTRACT NO. NCC8-38

Time Dependent Numerical Simulation

MATERIAL PROCESSING OF CONVECTION-DRIVEN FLOW FIELD AND TEMPERATURE DISTRIBUTION UNDER OBLIQUE GRAVITY

Prepared by R.J. Hung, Professor

Department of Mechanical and Aerospace Engineering

The University of Alabama in Huntsville

Huntsville, Alabama 35899

Abstract

A set of mathematical formulation is adopted to study vapor deposition from source materials driven by heat transfer process under normal and oblique directions of gravitational acceleration with extremely low pressure environment of 10^{-2} mm Hg. A series of time animation of the initiation and development of flow and temperature profiles during the course of vapor deposition has been obtained through the numerical computation. Computations show that the process of vapor deposition has been accomplished by the transfer of vapor through a fairly complicated flow pattern of recirculation under normal direction gravitational acceleration. It is obvious that there is no way to produce a homogeneous thin crystalline films with fine grains under such a complicated flow pattern of recirculation with a non-uniform temperature distribution under normal direction gravitational acceleration. There is no vapor deposition due to a stably stratified medium without convection for reverse normal direction gravitational acceleration. Vapor deposition under oblique direction gravitational acceleration introduces a reduced gravitational acceleration in vertical direction which is favorable to produce a homogenous thin crystalline films. However, oblique direction gravitational acceleration also induces an unfavorable gravitational acceleration along horizontal direction which is responsible to initiate a complicated flow pattern of recirculation. In other words, it is necessary to carry out vapor deposition under a reduced gravity in the future space shuttle experiments with extremely low pressure environment to process vapor deposition with a homogenous crystalline films with fine grains. Fluid mechanics simulation can be used as a tool to suggest most optimistic way of experiment with best setup to achieve the goal of processing best nonlinear optical materials.

I. Introduction

In recent years, a great deal of interest has been directed toward the use of organic materials in the development of higher efficiency optoelectronic devices. There is a myriad of possibilities among organics which allows a great deal of flexibility in the design of unique structures with a variety of functional objectives. The use of nonlinear optical (NLO) organic materials as thin film waveguides allows full exploitation of their desirable qualities by permitting long interaction lengths and large power densities with modest power input(Nayar and Winter, 1990). There are several methods in use to prepare thin films, such as Langmuir-Blodgett(Carter et al., 1988; Kajzar et al., 1983; Kajzar and Meissier, 1988), growth from sheared solution or melt(Thakur and Meyler, 1985; Thakur et al., 1986; Seymour et al., 1985), and melt growth between glass plates(Ledoux et al., 1986). This method, for preparing thin films, has shown some evidence that microgravity processing with extremely low pressure of 10^{-2} mm Hg may be beneficial.

Epitaxial growth on ordered organic and inorganic substrates and variations in processing conditions have been used to prepare highly oriented polydiacetylene and phthalocyanine films. The relationship of processing conditions to uniformity in thickness, degree of orientation, and nonlinear optical properties are very important. Also, improvements in fabrication techniques for growth of thin films by vapor deposition would be useful. Time variation of the initiation and formation of flow field and temperature distribution during the vapor deposition process under extremely low pressure environment can provide a better understanding in the framework to determine whether nonlinear optical thin films should be grown in space to improve uniformity in thickness and homogeneity if ground-based research and theoretical

studies indicate that this is feasible.

NASA Marshall Space Flight Center is currently engaged in the research of using a vapor deposition method to process nonlinear optical materials by growing thin crystalline films of diacetylene monomer(Paley et al., 1992). A better understanding of flow profiles and temperature distribution for vapor, which is produced from source material and propagates through the major driving mechanisms of heat transfer with natural convection and the diffusion process, can greatly enhance and improve the technique of nonlinear optical material processing.

In this study, an initiation and development of time-dependent, three-dimensional fluctuations of flow profiles and temperature distribution driven by heat transfer with a natural convection under normal and oblique directions of gravitational acceleration with extremely low pressure environment have been considered. Purpose of this study is to investigate the probability of processing vapor deposition under normal gravity with various directions to produce a homogenous thin crystalline films with fine grains. Results of present study will provide the critical guidelines for future space shuttle experiments. Size of container adopts in this simulation will be served directly to facilitate the infrastructures to be used for both ground-based and space shuttle experiments.

II. Mathematical Formulation

Governing equations, initial and boundary conditions for the present study of convection-driven material processing are illustrated.

(II-A) Governing Equations

Consider a co-axial cylinder with an inner radius of R_1 and an outer radius of R_2. The heights of the outer and inner cylinders are L_2, and $(L_2 - L_1)$, respectively. Figure 1 shows the geometrical configuration of the co-axial

cylinder. For the purpose of considering the mathematical formulation, cylindrical coordinates (r, θ, z) with a corresponding velocity components (u, v, w), and corresponding components of gravity acceleration (g_r, g_θ, g_z) is adopted. Figures 1(A) and 1(B) show the geometrical configuration of co-axial cylinder in the r-z plane and r-θ plane, respectively. There are two temperature zones in this co-axial cylinder. The external walls of the outer cylinder are surrounded by water jacket which maintains a constant temperature of 120° C while the walls of the inner cylinder keeps a constant temperature of 30° C. A low pressure air with the pressure of 10^{-2} mm H_g (= 1.333 N/m^2) is filled in the gap between the outer and inner walls of the co-axial cylinder. The flow profiles and temperature distributions of the low pressure air are mainly governed by the natural convection of the flow pattern in this problem. The governing equations can be shown as follows:

(a) Continuity Equation

$$\frac{1}{r}\frac{\partial}{\partial r}(ru) + \frac{1}{r}\frac{\partial v}{\partial \theta} + \frac{\partial w}{\partial z} = 0 \qquad (1)$$

(b) Momentum Equations

$$\rho\left(\frac{\partial u}{\partial t}+u\frac{\partial u}{\partial r}+\frac{v}{r}\frac{\partial u}{\partial \theta}-\frac{v^2}{r}+w\frac{\partial u}{\partial z}\right) = -\frac{\partial p}{\partial r}-\rho g_r[1-\beta(T-T_\infty)]$$

$$+\mu\left(\nabla^2 u-\frac{u}{r^2}-\frac{2}{r^2}\frac{\partial v}{\partial \theta}\right) \qquad (2)$$

$$\rho\left(\frac{\partial v}{\partial t}+u\frac{\partial v}{\partial r}+\frac{v}{r}\frac{\partial v}{\partial \theta}+\frac{uv}{r}+w\frac{\partial v}{\partial z}\right) = -\frac{1}{r}\frac{\partial p}{\partial \theta}$$

$$-\rho g_\theta[1-\beta(T-T_\infty)]+\mu\left(\nabla^2 v-\frac{v}{r^2}+\frac{2}{r^2}\frac{\partial u}{\partial \theta}\right) \qquad (3)$$

$$\rho\left(\frac{\partial w}{\partial t}+u\frac{\partial w}{\partial r}+\frac{v}{r}\frac{\partial w}{\partial \theta}+w\frac{\partial w}{\partial z}\right)=-\frac{\partial p}{\partial z}-\rho g_z[1-\beta(T-T_\infty)]+\mu\nabla^2 w \qquad (4)$$

where

$$\beta=\frac{1}{\rho_\infty}\left(\frac{\partial \rho}{\partial T}\right)_p \quad ,\nabla^2=\frac{1}{r}\frac{\partial}{\partial r}\left(r\frac{\partial}{\partial r}\right)+\frac{1}{r^2}\frac{\partial^2}{\partial \theta^2}+\frac{\partial^2}{\partial z^2}$$

and

$$(g_r, g_\theta, g_z) = g(\sin\psi\cos\theta, -\sin\psi\sin\theta, -\cos\psi)$$

(c) Energy Equation

$$\rho c_p\left(\frac{\partial T}{\partial t}+u\frac{\partial T}{\partial r}+\frac{v}{r}\frac{\partial T}{\partial \theta}+w\frac{\partial T}{\partial z}\right) = k\nabla^2 T \qquad (5)$$

Here, ρ, p, T, μ, k, and g denote density, pressure, temperature, viscous coefficient, heat conduction coefficient of air, and background gravity acceleration, respectively. ψ is the angle between the gravity vector and the axis of cylindrical cylinder. In this case, T_∞ and ρ_∞ stand both air temperature and density at the conditions of low pressure at 10^{-2} mm Hg and heat sink at the wall of the inner cylinder at T = 30° C. In these mathematical expressions, Boussinesq approximation is employed to formulate the relationship between local fluctuations of density and temperature through the thermal expansion coefficient β which replaces the equation of state.

(II-B) Initial and Boundary Conditions

The initial and boundary conditions have been assigned explicitly to solve governing equations (11) to (5) simultaneously.

(a) Initial Condition

At time t = 0, all the flow profiles vanish, i.e.

$$u = v = w = 0 \qquad \text{everywhere} \qquad (6)$$

The temperature distribution of fluid inside the container is 30°C, and

outside the container is expressed by

$$T = 30^\circ C \quad \text{at } r \le R_1,\ 0 \le \theta \le 2\pi, \quad (L_2 - L_1) \le z \le L_2 \tag{7}$$

$$T = 120^\circ C \quad \text{at} \quad z \le 0;\ r \ge 0;\ 0 \le \theta \le 2\pi \tag{8}$$

$$\text{at } z \ge L_2;\ r \ge 0;\ 0 \le \theta \le 2\pi \tag{9}$$

$$\text{at} \quad 0 \le z \le L_2;\ r \ge R_2;\ 0 \le \theta \le 2\pi \tag{10}$$

Pressure profile inside the container is

$$p = 10^{-2} \text{ mm Hg} = 1.333 \text{ N/m}^2 \tag{11}$$

(b) Boundary Conditions

At time $t > 0$, temperature distribution shown in Equations (7) to (10), and pressure profile shown in Equation (11) remain to be true.

For flow profiles, no penetration and no slip conditions along the surfaces of solid wall shall apply, namely

$$u = v = w = 0 \tag{12}$$

along the surfaces of $r = R_1,\ 0 \le \theta \le 2\pi,\ (L_2 - L_1) \le z \le L_2$; (13)

$$r \ge 0,\ 0 \le \theta \le 2\pi,\ z = 0; \tag{14}$$

$$r \ge 0,\ 0 \le \theta \le 2\pi,\ z = L_2; \text{ and} \tag{15}$$

$$r = R_2,\ 0 \le \theta \le 2\pi,\ 0 \le z \le L_2 \tag{16}$$

A co-axial cylindrical container designed to be used directly in the future space shuttle experiments, illustrated in Figure 1, with following specifications are assigned: L_1=6 cm, L_2=12 cm, R_1=0.9 cm, and R_2=1.5 cm. Following physical parameters were used: gravity acceleration g_o = 9.81 m/s^2, air pressure=1.333 N/m^2, air density=1.71x10^{-5} kg/m^3, air viscosity coefficient=2.0x10^{-5} m^2/s, coefficient of thermal expansion for air (β)=2.87x10^{-3} 1/K and Prandtl number for air=0.72.

to investigate the most significant driving parameters in this study, let us consider the inertia, buoyancy and viscous terms,

$$w \bullet w/L \sim g_z \beta \Delta T \sim \nu W/\delta_T^2 \tag{17}$$

respectively, which are on the same order of magnitude in momentum equation shown in Equation (4); and convection and conduction terms,

$$w/L\Delta T \sim \alpha\ \Delta T/\delta_T^2 \tag{18}$$

respectively, which are also on the same order of magnitude in energy equation shown in Equation (5). Here, δ_T is the thermal boundary layer thickness; L is the height of container along z-axis; $\nu = \mu/\rho$ is the kinematic viscosity; and $\alpha = k/\rho c_p$ is the thermal diffusivity. From convection and conduction terms in Equation (18); from inertia and buoyancy terms in Equation (17); and from bouyancy and viscous terms in Equation (17), we can obtain induced convective velocity of flows as follows:

$$w \sim \alpha L/\delta_T^2 \tag{19}$$

$$w \sim (g_z \beta L \Delta T)^{1/2} \tag{20}$$

and

$$w \sim (g_z \beta \delta_T^2 \Delta T)/\nu \tag{21}$$

respectively. By equating Equations (19) and (21), we have the relationship of

$$\delta_T/L \sim Ra^{-1/4} \tag{22}$$

based on the balance between bouyancy and viscous forces. By equating Equations (19) and 20), we have another relationship of

$$\delta_T/L \sim (Ra \cdot Pr)^{-1/4} \sim (Gr)^{-1/4}\ (Pr)^{-1/2} \tag{23}$$

based on the balance between buoyancy and inertia forces. Here Reyleigh number (Ra), Grashof number (Gr), and Prandtl number (Pr) are defined as

$$Ra = g_z \beta L^3 \Delta T/\alpha\nu \tag{24}$$

$$Gr = g_z \beta L^3 \Delta T/\nu^2 = Ra/Pr \tag{25}$$

and

$$Pr = \nu/\alpha \tag{26}$$

Since the heat transfer coefficient scales as k/δ_T (Bejan, 1995), the Nusselt number (Nu) varies as

$$Nu = hL/k \sim Ra^{1/4} \tag{27}$$

from Equation (22) based on the balance between buoyancy and viscous forces; and Nu varies as

$$Nu \sim (Ra \cdot Pr)^{1/4} \sim (Gr)^{1/4} (Pr)^{1/2} \qquad (28)$$

As indicated by Bejan (1995), both theoretical and laboratory measurement show that Equation (27) is particularly applicable for $Pr > 1$ fluids, while Equation (28) is dominated by $Pr << 1$ fluids. For the case of present research, the dominated parameter is Rayleigh number rather than Grashof number (Bejan, 1995).

In this study, it is shown later in the numerical simulation that the maximum induced flow velocity driven by convection is 0.2 m/s. Reynolds number ($Re = wD/\nu$ where D is the diameter of container) for the flow pattern based on this maximum flow velocity is 150 which is far below the possibility to produce turbulent flow fields. Grashof number (Gr) and Rayleigh number (Ra) for the present case study are 8×10^6 and 7.8×10^6, respectively, under normal gravity condition. It is well-known that the condition for the onset of convection with fluid layers heated from below is $Ra > 1.1 \times 10^3$ (Bejan, 1995). In other words, the total elimination of the onset of induced convection with the proposed size of container is possible only to perform the space experiment of material processing under the reduced gravity environment of 10^{-4} g_o and below.

III. Mathematical Simulation of Flow Profiles and Temperature Distributions

Equations (1) to (5) subject to initial conditions shown in Equations (8) to (11), and boundary conditions shown in Equations (12) to (16), have been used to solve time-dependent, three-dimensional flow profiles and temperature distributions numerically. The computer algorithms employed in this study have been developed and illustrated in our earlier studies (Hung et al., 1992 a, b, c, d; 1993 a, b; 1994 a, b, c, d, e), and will not be repeated in this paper. The time step is determined automatically based on the size of grid points and the velocity of flow fields. As the thickness of boundary layer is inversely

proportional to the square root of Reynolds number, size of grid points shall be adjusted according to the flow fields of Reynolds number. In other words, the size of grid points shall be smaller as the flow fields of Reynolds number becomes greater. Fail of adjusting the size of grid points based on the increasing of Reynolds number will result in the numerical instability to the extreme severity of the local oscillations (Kitchen et al., 1978; Kitchens, 1980). Special care shall be attempted to eliminate these numerical instabilities by properly adjusting the size of grid points which eventually contribute to the adjustment of time steps. It is needless to say that the development of a real physical instability will certainly occur at the higher Reynolds number because of less viscosity effect contributing to the damping of flow disturbances. It is utterly important for us to distinguish the differences between numerical and real physical instabilities, particularly for the flows with high Reynolds number.

In this study, two sets of the size of grids, with the grids of 17 X 34 X 42 and 23 X 34 X 82 along (r,θ,z) coordinates, have been designed to carry out numerical computations. As the Reynolds number of 150 with maximum induced velocity of 0.2 m/s for the present case, there is no difference concluded for numerical results obtained for either grids chosen. By using the grids of 17 X 34 X 42 in the computation of flows with higher Reynolds number, such as $Re \geq 1500$ with induced velocity of 2.0 m/s and higher. An extremely severe numerical instabilities of flow field is resulted.

With grids of 17x34x42, the average time step determined from the size of grid points and velocity of flow fields is 0.0007 s, while the CPU time required by the Supercomputer CRAY II to execute one time step is 3.019 s. The total CPU time consumed for each of the three cases in this study is 12000 s CRAY II computer time.

In this study, direction of background gravity along three different directions with ψ = 0°, 45° and 180° along the r-z plane with θ = 0° are chosen as the examples to investigate the characteristics of convection-driven flow and temperature profiles. Results of present study will be used as the guidelines to facilitate the space experiments to be carried out with the container specified in this paper.

Various references have been cited by Bejan (1995) in the study of induced convective heat transfer with fluid layers heated from below, top, side, oblique, etc., under the normal atmospheric pressure. As mentioned in the Introduction, purpose of this study is to investigate time variation of the initiation and formation of flow field and temperature distribution during the vapor deposition process to determine the possibility of processing nonlinear optical thin films under the extremely low pressure environment of 10^{-2} mm Hg. Study of induced convective heat transfer under such a low pressure environment has not been done earlier, and there is no available literature for comparison. However, there is a qualitative agreement of both flow profiles and temperature distribution for the induced convections under normal atmosphere pressure and 10^{-2} mm Hg low pressure.

(A) Convection Driven by Normal Direction (ψ=0°) Gravitational Acceleration

Time animation of the development of flow fields with normal direction (ψ= 0°) gravitational acceleration is illustrated in Figure 2 for convection-induced flow vectors (in terms of directions and magnitudes of convection induced-flow velocities) in r-z plane. The maximum velocity for each subfigure is specified separately at the corresponding subfigure. For the convenience of comparison, 8 subfigures with time sequence at t= 0.22, 0.58, 1.29, 1.72, 1.99, 2.39, 2.70, and 3.10 s throughout this paper are illustrated. Following results are concluded in these series of subfigures in Figure 2: (a) A convection induced downward flow

toward the bottom of outer cylinder with inflow stream is initiated at the bottom of central column at time $t<0.2$ s (not shown). (b) A convection induced downward flow along the surface of cylindrical central column with inflow from the surface of outer cylinder toward the surface of cylindrical central column (at upper section of container within the slender gap between co-axial cylinders) is also initiated during the time period of $0.2\ s<t<0.4$ s. (c) A convection induced flow patterns of upward flow along the surface of outer cylinder and downward flow along the surface of inner cylinder (central column) are gradually formed (at upper section of container within the slender gap between co-axial cylinders) with intensified flow velocities accompanied by a stream of inflow from the surface of outer cylinder to inner cylinder during the time period of $0.2\ s<t<0.9$ s. (d) A tendency of convection induced inflow pattern toward center of axial coordinate at upper section of container with heights in $z>2.7$ cm, and outflow pattern toward the surface of outer cylinder at lower section of container with heights in $z<2.7$ cm are gradually formed for time $t>0.9$ s. (e) It shows a convection induced flow pattern of two recirculation flows with centers at $(r_c,z_c)=(\pm 1.9,\ 2.7)$ cm where r_c and z_c denote the centers of recirculation flow along r- and z- coordinates, respectively. Direction of left-hand-side convection induced recirculation flow is clockwise while that of the right-hand-side convection induced recirculation flow is counter-clockwise circulation for time $t>1.3$ s.

For the purpose to illustrate the flow patterns of convection induced inflow and outflow, Figures 3 and 4 show time animation of initiation and development of convection induced inflow in the region below the central column (at $z=5.55$ cm), and convection induced outflow in the region near the bottom of outer cylinder (at $z=0.45$ cm), respectively. Figures 3 and 4 also show convection induced flow vectors (in terms of directions and magnitudes of induced

flow velocities) in r-θ (x-y) plane. The maximum velocity for each subfigure is also specified separately at the corresponding subfigure. It is interesting to emphasize that there is an induced inflow region with flow from the surface of outer cylinder inward toward the central direction with location at the upper section of container with heights in $z>2.7$ cm. It is also an induced outflow region with flow from the center of axial coordinate outward toward the surface of outer cylinder at the lower section of container with heights in $z<2.7$ cm. Before the induced flow is developed to such a clear-cut regions of upper part with inflow and lowerpart with outflow for the flow approaching to steady-state case, there is an induced transient flow pattern at the beginning of flow formation. Figure 3 shows that there is an induced temporary outflow formed at the exterior region of container near the surface of outer cylinder at the very beginning of flow initiation. This induced temporary flow region disappears quickly as the flow development near the steady-state. Obviously, the major vapor deposition at the bottom surface of the central column are contributed by the induced inflow from exterior flow zones which were brought upward along the surface of outer cylinder from the evaporation of source materials stored at the bottom surface of outer cylinder. In other words, the flow analysis indicates that the vapor deposition at the bottom surface of central column was not a result of direct straight upward diffusion from the evaporation of source materials stored at the bottom surface of outer cylinder. It is rather a vapor deposition process resulted from a fairly complicated induced flow pattern of recirculation.

Figure 5 shows a time animation of the initiation and formation of temperature profiles due to induced convection in r-z plane at $\theta=0°$ and 180° during the course of the entire induced flow region development. The curves show in Figure 5 are the isothermal lines with values indicated with temperature in

°C at the corresponding locations. Comparisons of Figures 2 to 5 can be concluded as follows: (a) At time t=o (not shown), there is a very sharp temperature varying from 30 to 120 °C in a fairly thin layer. (b) An initiation of downward induced flow from the bottom of central column toward the bottom of outer cylinder immediately creates a gradually expanding positive temperature gradient along the downward directions for time t>0.1 s. (c) A flow pattern of induced inflow from the surface of outer cylinder toward the center of axial coordinate promotes a parabolic shape temperature profile with downside tip point around the center of axial coordinate due to the induced downward cold streams from the bottom of central column for time t>0.1 s. (d) An induced upward profile of temperature distribution at the exterior region of container around the surface of outer cylinder is a result of induced upward flow pattern along the corresponding surface. (e) An induced downward elongation profile of temperature distribution immediately around the neighborhood of the surface of inner cylinder (central column), is a result of induced downward flow pattern along the corresponding surface.

(B) Convection Driven by Reverse Normal Direction (ψ=180°) Gravitational Acceleration

Time animation of the development of induced flow fields associated with reverse normal direction (ψ=180°) gravitational acceleration is illustrated in Figure 6 for convection induced flow vectors (in terms of directions and magnitude of induced flow velocities) in r-z plane. The maximum velocity for each subfigure is specified separately at the corresponding subfigure. This problem can be divided into two sections for flow fields induced by the reverse normal direction (ψ=180°) gravitational acceleration. For z > 6 cm, the problem associated with horizontal heating from the outer walls of cylinder toward the central wall within a narrow cylindrical slit of space. For z < 6 cm, this is

a typical problem of vertical heating from the top (downward gravity direction). As the source material is located at the surface of z = 0, and the location of vapor deposition is designed at bottom horizontal surface of central column at z = 6 cm, the flow profile in z > 6 cm has very little effect on the flow pattern of vapor deposition. Thus, we can ignore the flow profiles induced within a narrow cylindrical slit of space. As to the flow in z < 6 cm, Figure 6 shows a stably stratified medium and natural convection is completely prohibited.

For the purpose to illustrate the flow patterns of inflow and outflow induced by the reverse normal direction (ψ=180°) gravitational acceleration. Figures 7 and 8 show time animation of initiation and development of outflow in the region below the central column (at z = 5.55 cm), and inflow in the region near the bottom of outer cylinder (at z = 0.45 cm), respectively. Figures 7 and 8 also show flow vectors (in terms of directions and magnitudes of induced flow velocities) in r-θ (x-y) plane. The maximum velocity for each subfigure is specified separately at the corresponding subfigure. Comparison of Figures 6,7, and 8 show some interesting results as follows: (a) Practically, there is no induced flow field for natural convection along the vertical direction and only a stratified medium is shown in the r-z plane for z < 6 cm due to the phenomena of vertical heating from the top (downward gravity direction). (b) There is a very small induced flow along horizontal direction in r-θ plane for z < 6 cm due to the heating from side walls, a slightly greater magnitude at top than that at bottom in this region for effect of low temperature central column at z > 6 cm.

Figure 9 shows a time animation of the initiation and formation of temperature profiles driven by the reverse normal direction (ψ=180°) gravitational acceleration in r-z plane at θ=0° and 180° during the course of the entire flow region development. The curves show in Figure 9 are the isothermal lines with values indicated the temperature in °C at the corresponding locations.

Again, it shows a clear two regions. For region of $z > 6$ cm, horizontal heating from side wall drives the convective flow toward the central wall within a narrow cylindrical slit which shows a series of isothermal curves with temperature decreasing from side wall toward the wall along central column. As indicated earlier, this region is not important in our study of vapor deposition from source materials located at the surface of $z = 0$ transferring to the bottom of central column at $z = 6$ cm. There is not much variation in the dynamics of temperature distribution for the region of $z < 6$ cm because the region is filled with stably stratified medium, and the natural convection is completely prohibited.

(C) Convection Driven by 45° Oblique Direction Gravitational Acceleration

In this case, 45° oblique gravitational acceleration is applied along the r-z plane with θ=0°. In other words, induced flow profile, shown in Figure 10 with r-z plane at θ=0° and 180°, is an illustration of convective flow induced by a vector summation of gravitational acceleration with a magnitude of horizontal 0.707 g_o ($g_o$sin 45°) rightward, and vertical 0.707 g_o ($g_o$cos 45°) downward components. On the otherhand, induced flow profile, shown in Figure 11 with r-z plane at θ=90° and 270°, shows convective flow induced by a reduced gravity acceleration with a magnitude of 0.707 g_o downward component.

Comparison of Figures 2 and 10 show the following results: (a) A downward flow toward the bottom of the outer cylinder with inflow stream is initiated at the bottom of central column for both normal and oblique gravitational acceleration at time $t < 0.2$ s. (b) A downward flow along the surface of cylindrical central column with inflow from the surface of outer cylinder toward the surface of cylindrical central column (at upper section of container within the slender gap between co-axial cylinders) is also initiated for both normal and oblique gravitational acceleration during the time period of $0.2 \text{ s} < t < 0.4$ s. (c) A

flow patterns of upward flow along the surface of left-side outer cylinder and downward flow along the surface of inner cylinder (central column) and right-side outer cylinder are gradually formed (at upper section of container within the slender gap between co-axial cylinders) with intensified flow velocities accompanied by a stream of inflow at left-side from the surface of outer cylinder to inner cylinder, and outflow at right-side from the surface of inner cylinder to outer cylinder driven by 45° oblique direction gravitational acceleration during the time period of $0.2\ s < t < 0.9\ s$. This asymmetric flow profile is quite different from the symmetric flow profile resulted from ψ=0° direction normal gravity acceleration. (d) A tendency of inflow pattern at left-side, and outflow at right-side, for height in $z > 1.2$ cm; and outflow at left-side, and inflow at right-side, for height in $z < 1.2$ cm are gradually formed for time $t > 0.9$ s. (e) It shows a flow pattern of asymmetric recirculation flow with center at $(r_c, z_c)=(0.6, 1.2)$ cm where r_c and z_c denotes the center of recirculation flow along r- and z- coordinates, respectively. Direction of recirculation flow is clock-wise for time $t > 1.2$ s.

In contrast to Figure 10 for induced asymmetric flow profile in r-z plane at θ=0°-180° due to ψ=45° oblique direction gravitational acceleration, Figure 11 shows an induced symmetric flow profile in r-z plane at θ=90°-270° due to a reduced 0.707 g_o gravity acceleration in downward direction. Comparison of Figures 2 and 11 show the differences in induced flow fields driven by normal (1 g_o) and reduced (0.707 g_o) gravitational accelerations. Major differences are as follows: (a) Upward motions along the surface of outer cylinder are shown for flow induced by the normal gravity acceleration, while the similar upward motions around the central axis of the cylinder are resulted for flow induced by the reduced gravity acceleration. (b) Downward motions around the central axis of cylinder are illustrated for flow induced by normal gravity acceleration, while

the similar downward motion along the surface of outer cylinder are resulted for flow induced by the reduced gravity. (c) There are two recirculation flows generated with centers at $(r_c, z_c) = (\pm 1.9, 2.7)$ cm, and at $(r_c, z_c) = (\pm 0.8, 3.2)$ cm for flows induced by normal and reduced gravity accelerations, respectively. (d) Directions of left-hand side and right-hand side recirculation flows are clockwise and counter clockwise, respectively, for flows induced by normal gravity, while that of the directions of recirculation flows for the similar sides are counter clockwise and clockwise, respectively, for flows induced by reduced gravity acceleration. These results show a very important result that the reduced gravity can help in promoting a direct transport of source materials at the bottom of outer cylinder to the location of vapor deposition at the bottom of central column without going through the complicated flow profiles of transport process.

For the purpose to illustrate the flow patterns of inflow and outflow, Figures 12 and 13 show time animation of initiation and development of mostly outflow in the region right below the central column (at $z = 5.55$ cm), and mostly inflow in the region near the bottom of outer cylinder (at $z = 0.45$ cm), respectively. Figures 12 and 13 also show flow vectors (in terms of directions and magnitudes of induced flow velocities) in r-θ (x-y) plane. The maximum velocity for each subfigure is specified separately at the corresponding subfigure. It is interesting to emphasize that there is a flow region with mostly outflow for flow from the central axis of cylinder outward toward the direction of the surface of outer cylinder with location at the upper section of container with heights in $z > 0.8$ cm. It is also a flow region with mostly inflow for flow from the surface of outer cylinder inward toward the central axis of cylinder at the lower section of container with heights in $z < 0.8$ cm. Because horizontal component with a magnitude of 0.77 g_o gravitational

acceleration contributes to the initiation of very complicated flow profiles, shown in Figures 12 and 13, there are inflow component shown in height $z > 0.8$ cm, and outflow component shown in height $z < 0.8$ cm in the range between $135° < \theta < 225°$. In other words, because of the presence of horizontal component gravitational acceleration due to oblique direction gravity acceleration, the vapor deposition at the bottom surface of the central column are contributed by the mixing of (a) inflow from external flow zones in the range between $135° < \theta < 225°$ which were brought upward along the surface of outer cylinder from the evaporation of source materials stored at the bottom surface of outer cylinder, and (b) the direct transport from the source materials which were upward to the location of vapor deposition in the rest of the ranges. In other words, the flow analysis indicates that the vapor deposition at the bottom surface of central column was able to secure a complete result of direct straight upward diffusion from the evaporation of source materials stored at the bottom surface of outer cylinder exposed to oblique direction gravitational acceleration. In other words, obliqued direction gravitational acceleration can not secure a better quality vapor deposition because the presence of horizontal component of gravitational acceleration.

Figures 14 and 15 show the time animation of the initiation and formation of temperature profiles in r-z plane at θ=0°-180°, and at θ=90°-270°, respectively during the course of the entire flow region development under oblique direction gravitational acceleration. Figure 14 shows the temporal variation of isothermal lines resulted from the combination of rightward and downward gravity accelerations. It shows clearly the initiation and development of the progressing of isothermal lines following the trend of a combination of rightward and downward movement. Comparison of Figure 10 for the velocity profile and Figure 14 for the temperature profile illustrate a very interesting similarity in these two groups

of curves.

Figure 15 shows the similar temporal variation of isothermal lines from another angle point of view which was resulted from a reduced gravity acceleration with a magnitude of 0.707 g_o. Initiation and development of cone shape temperature profile is resulted from a direct upward induced flow from bottom surface of outer cylinder transporting toward bottom surface of central column. These temperature profiles shown in Figure 15, and flow profile shown in Figure 11, suggest a very promising indication that the vapor deposition under a reduced gravity environment may be able to promote material processing of vapor deposition with a homogeneous crystalline films with fine grains.

IV. Discussion and Conclusion

In this study, mathematical formulations of the initiation and development of fluid profiles and temperature distributions driven by the heat transfer process of natural convection under normal and oblique directions of gravitational acceleration with extremely low pressure environment have been carried out. Purpose of present study is to investigate the characteristics of vapor deposition under low pressure environment to be used for promoting the process of nonlinear optical materials by growing thin crystalline films of diacetylene monomer(Nayer and Winter, 1990). Numerical computation of a full set of nonlinear fluid dynamics show that vapor deposition process has to be accomplished through a fairly complicated flow patterns of recirculation under normal gravity environment both in normal and oblique directions which are the major driving forces to induce natural convection in low pressure environment. For the case of natural convection under normal gravitational acceleration with oblique direction along a plane perpendicular to the gravity acceleration, result shows a possibility to induce a simple direct updraft motion to transport source materials from the location of storage to the location of vapor deposition under

a reduced gravitational acceleration. Since the oblique direction gravitational acceleration is always accompanied with the component of gravitational acceleration in horizontal direction, the existence of horizontal component is responsible for the generation of complicated flow patterns with recirculation. It can be anticipated that there is no way to produce a homogeneous thin crystalline films with fine grains under such a complicated flow patterns of recirculation with a nonuniform temperature distributing in normal gravity environment. This study suggests that it is necessary to adopt an unique environment with microgravity to eliminate natural convection. In so doing, we can carry out an experiment which can simplify the flow pattern and reach a goal to produce a homogeneous thin films with fine grains in the future space experiments. Numerical study of fluid mechanics computation can be used to facilitate most optimistic way of experiment with best setup to achieve the goal of processing best quality nonlinear optical materials in the future space experiments.

Acknowledgement

The authors appreciate the support received from the National Aeronautics and Space Administration through the NASA Contract NCC8-38. They would like to express their gratitude to Donald D. Frazier and Mark S. Paley of NASA Marshall Space Flight Center for the stimulating discussions during the course of present study.

References

Bejan, A., (1995) Convection Heat Transfer, 2nd Ed., Wiley, New York, pp. 623.

Carter, G.M., Chen, Y.J., and Tripathy, S.K., (1988) Appli. Phys. Lett.,43, 891.

Hung, R.J., K.L. Shyu, and C.C. Lee (1992a) Journal of Propulsion and Power, 8, 778-785.

Hung, R.J., K.L. Shyu, and C.C. Lee (1992b) Journal of Spacecraft and Rockets, 29, 523-528.

Hung, R.J., C.C. Lee, and F.W. Leslie (1992c) Journal of Guidance, Control and Dynamics, 15, 817-824.

Hung, R.J., C.C. Lee, and F.W. Leslie (1992d) Journal of Fluids and Structures, 6, 493-522.

Hung, R.J., C.C. Lee, and F.W. Leslie (1993a) Transaction of the Japan Society for Aeronautical and Space Sciences, 35, 187-207.

Hung, R.J., C.C. Lee, and F.W. Leslie (1993b) Journal of Aerospace Engineering, 207, 105-120.

Hung, R.J., H.L. Pan, and F.W. Leslie (1994a) Fluid dynamics Research, 14, 29-51.

Hung, R.J., H.L. Pan, and F.W. Leslie (1994b) Journal of Flight Sciences and Space Research, 18, 195-202.

Hung, R.J., H.L. Pan, and Y.T. Long (1994c) Acta Mechanica Sinica, 10, 367-381.

Hung, R.J., H.L. Pan, and Y.T. Long (1994d) Cryogenics, 34, 641-648.

Hung, R.J., Y.T. Long, and H.L. Pan (1994e) Transactions of Japan Society for Aeronautics and Space Sciences, 37, 217-234.

Kajzar, F., Meissier, J., Zyss, J., and Ledoux, I.,(1983) Opt. Commun.,45, 133.

Kajzar, F., and Messier, J., (1988) Thin Solid Films,132, 11.

Kitchens, C.W., N. Gerber, and R. Sedney (1978) Journal of Spacecraft and Rockets, 15, 348-354.

Kitchens, C.W. Jr. (1980) AIAA Journal, 18, 929-934.

Ledoux, I., Josse, D., Vidakovic, P., and Zyss, J., (1986) Optical Engineering,27(1), 49.

Nayar, B.K., and Winter, C.S., (1990) Optical and Quantum Electronics,22, 297.

Paley, M.S., Frazier, D.O., Abeledeyem, H., McManus, S.P., and Zutant, S.E., (1992) J. American Chemical Society,114, 3247-3251.

Seynour, R.J., Carter, G.M., Chen, Y.J., Elman, B.S., Rubner, M.E., Thakur, M.K., and Tripathy, S.K., (1985) SPIE Proceedings,567, 56.

Thakur, M., and Meyler, S., (1985) Macromolecules,18, 2341.

Thakur, M., Carter, G.M., Meyler, S., and Hryniewicz, H., (1986) Polymer Preprints, 27 (1), 49.

Figure Captions

Figure 1 Geometrical illustration of co-axial cylinders to be used for mathematical modeling, (A) in r-z plane, and (B) in r-θ plane.

Figure 2 Flow profile initiation and development in r-z plane at θ=0 ° and 180° under normal direction (ψ=0°) gravitational acceleration.

Figure 3 Flow profile initiation and development in r-θ plane at z = 5.55 cm under normal direction (ψ=0°) gravitational acceleration.

Figure 4 Flow profile initiation and development in r-θ plane at z = 0.45 cm under normal direction (ψ=0°) gravitational acceleration.

Figure 5 Initiation and formation of temperature profile in r-z plane at θ=0° and 180° under normal direction (ψ=0°) gravitational acceleration.

Figure 6 Flow profile initiation and development in r-z plane at θ=0° and 180° under reverse normal direction (ψ=180°) gravitational acceleration.

Figure 7 Flow profile initiation and development in r-θ plane at z = 5.55 cm under reverse normal direction (ψ=180°) gravitational acceleration.

Figure 8 Flow profile initiation and development in r-θ plane at z = 0.45 cm under reverse normal direction (ψ=180°) gravitational acceleration.

Figure 9 Initiation and formation of temperature profile in r-z plane at θ=0° and 180° under reverse normal direction (ψ=180°) gravitational acceleration.

Figure 10 Flow profile initiation and development in r-z plane at θ=0° and 180° under oblique direction (ψ=45°) gravitational acceleration.

Figure 11 Flow profile initiation and development in r-z plane at θ=90° and 270° under oblique direction (ψ=45°) gravitational acceleration.

Figure 12 Flow profile initiation and development in r-θ plane at z = 5.55 cm under oblique direction (ψ=45°) gravitational acceleration.

Figure 13 Flow profile initiation and development in r-θ plane at z = 0.45 cm

under oblique direction (ψ=45°) gravitational acceleration.

Figure 14 Initiation and formation of temperature profile in r-z plane at θ=0° and 180° under oblique direction (ψ=45°) gravitational acceleration,

Figure 15 Initiation and formation of temperature profile in r-z plane at θ=90° and 270° under oblique direction (ψ=45°) gravitational acceleration

(A) r - Z Plane

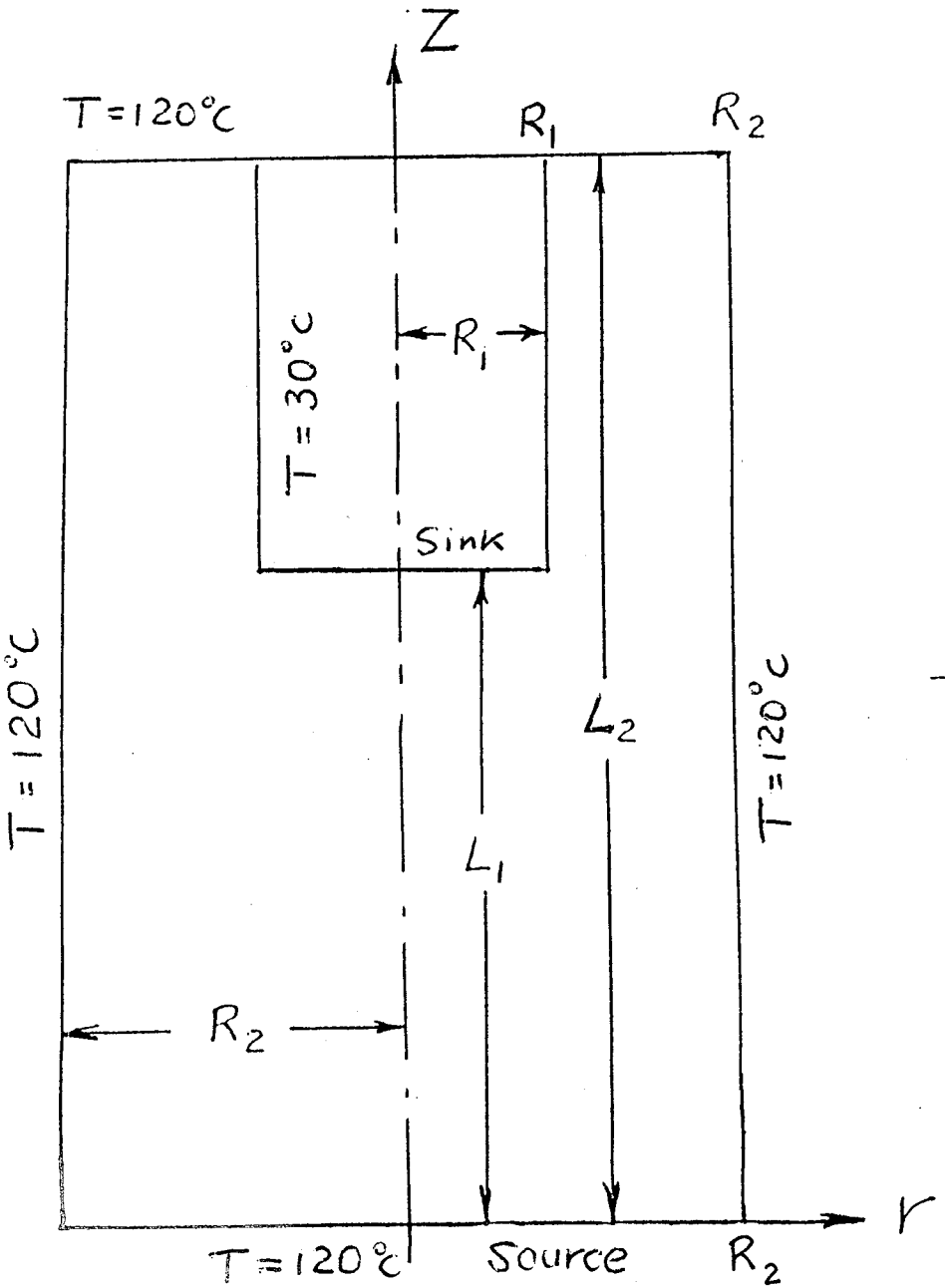

(B) r - θ Plane

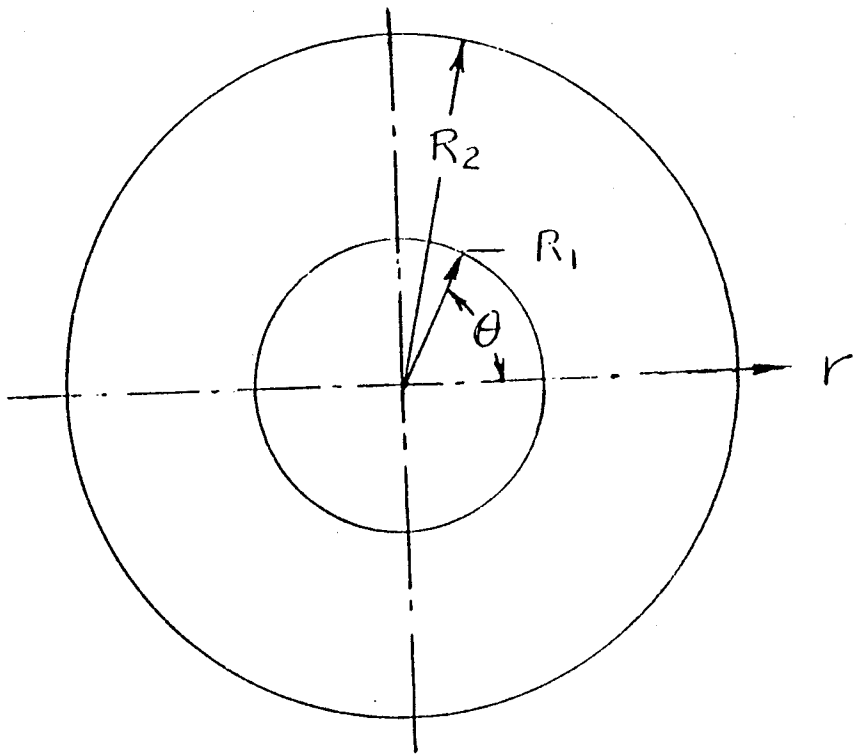

Fig. 1

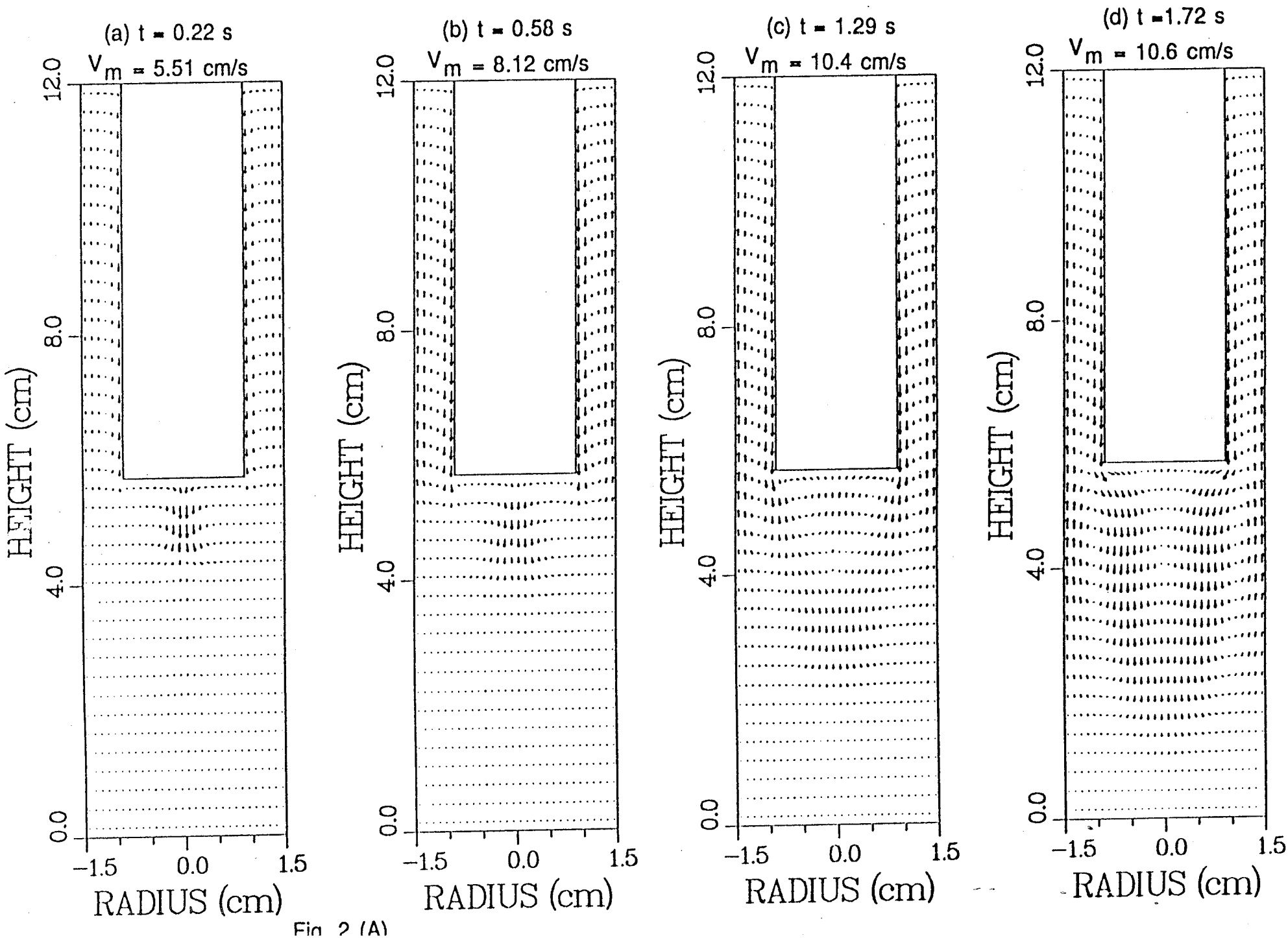
Flow Profile Initiation and Development in r - z Plane at θ = 0° - 180°, ψ = 0°
(a) t = 0.22 s
V_m = 5.51 cm/s
(b) t = 0.58 s
V_m = 8.12 cm/s
(c) t = 1.29 s
V_m = 10.4 cm/s
(d) t = 1.72 s
V_m = 10.6 cm/s
HEIGHT (cm)
RADIUS (cm)
0.0
4.0
8.0
12.0
−1.5
0.0
1.5

Fig. 2 (A)

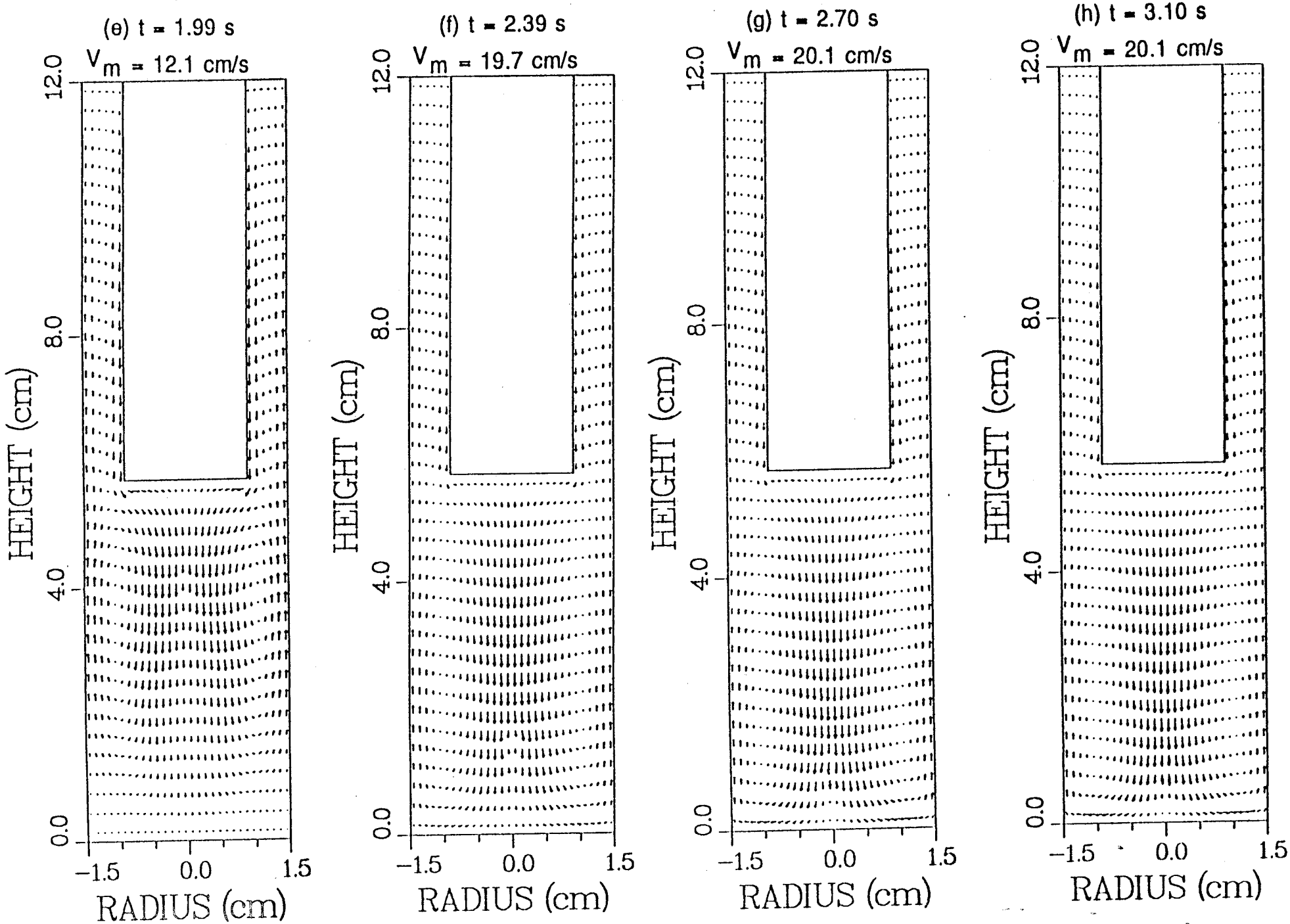
Flow Profile Initiation and Development in r - z Plane at θ = 0° - 180°, ψ = 0°
(e) t = 1.99 s
V_m = 12.1 cm/s
(f) t = 2.39 s
V_m = 19.7 cm/s
(g) t = 2.70 s
V_m = 20.1 cm/s
(h) t = 3.10 s
V_m = 20.1 cm/s
HEIGHT (cm)
12.0
8.0
4.0
0.0
−1.5
0.0
1.5
RADIUS (cm)

Fig. 2 (B)

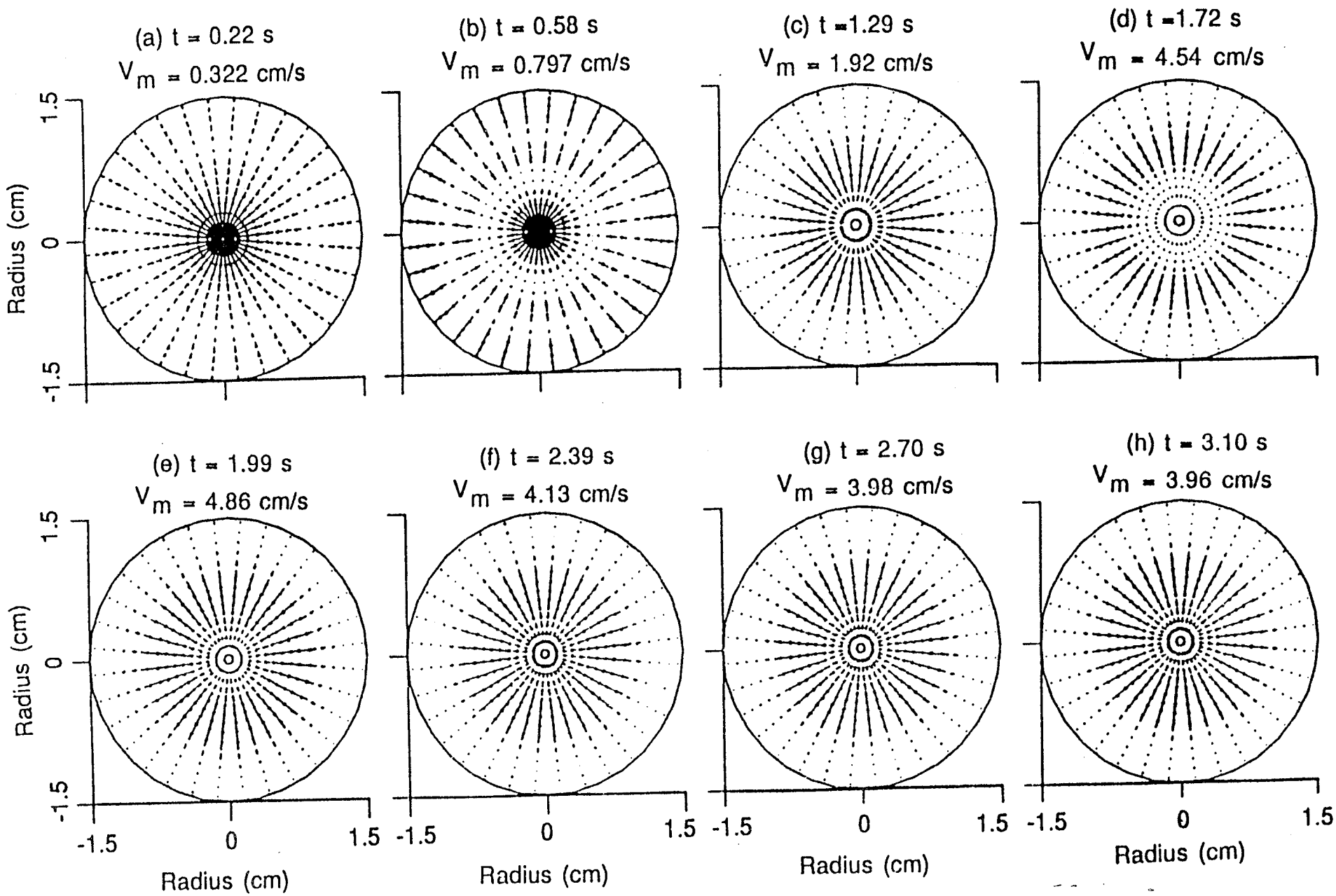
Flow Profile Initiation and Development in r - θ Plane at z = 5.55 cm, ψ = 0°
(a) t = 0.22 s
V_m = 0.322 cm/s
(b) t = 0.58 s
V_m = 0.797 cm/s
(c) t = 1.29 s
V_m = 1.92 cm/s
(d) t = 1.72 s
V_m = 4.54 cm/s
(e) t = 1.99 s
V_m = 4.86 cm/s
(f) t = 2.39 s
V_m = 4.13 cm/s
(g) t = 2.70 s
V_m = 3.98 cm/s
(h) t = 3.10 s
V_m = 3.96 cm/s
Radius (cm)
1.5
0
-1.5
Radius (cm)

Fig. 3

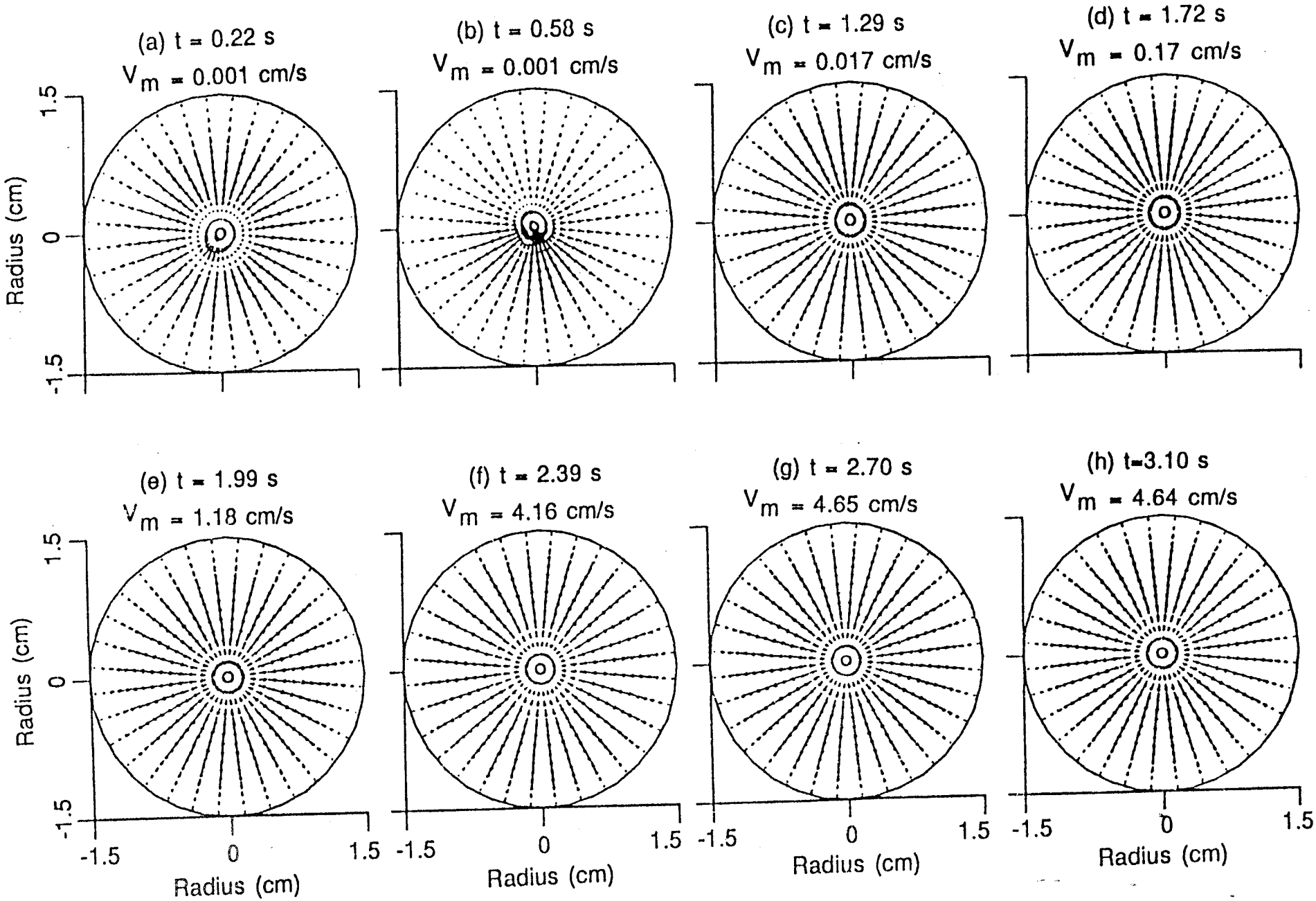
Flow Profile Initiation and Development in r - θ Plane at z = 0.45 cm, ψ = 00
(a) t = 0.22 s
Vm = 0.001 cm/s
(b) t = 0.58 s
Vm = 0.001 cm/s
(c) t = 1.29 s
Vm = 0.017 cm/s
(d) t = 1.72 s
Vm = 0.17 cm/s
(e) t = 1.99 s
Vm = 1.18 cm/s
(f) t = 2.39 s
Vm = 4.16 cm/s
(g) t = 2.70 s
Vm = 4.65 cm/s
(h) t=3.10 s
Vm = 4.64 cm/s
Radius (cm)
1.5
0
-1.5
Radius (cm)

Fig. 4

Initiation and Formatiom of Temperature Profile in r - z Plane at $\theta = 0^{o} - 180^{o}$, $\psi = 0^{o}$

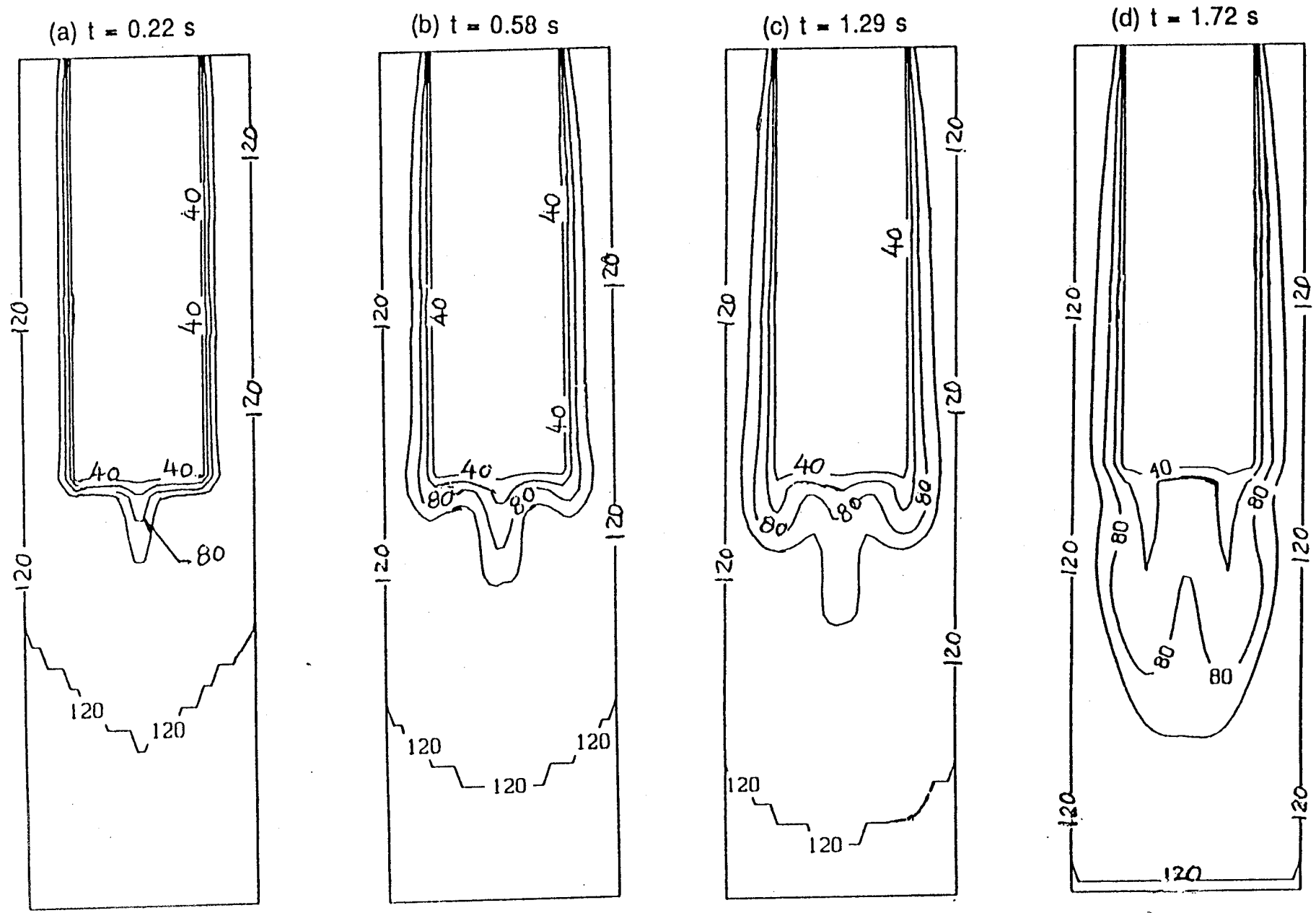

Fig. 5 (A)

Initiation and Formatiom of Temperature Profile in r - z Plane at $\theta = 0^{o} - 180^{o}$, $\psi = 0^{o}$

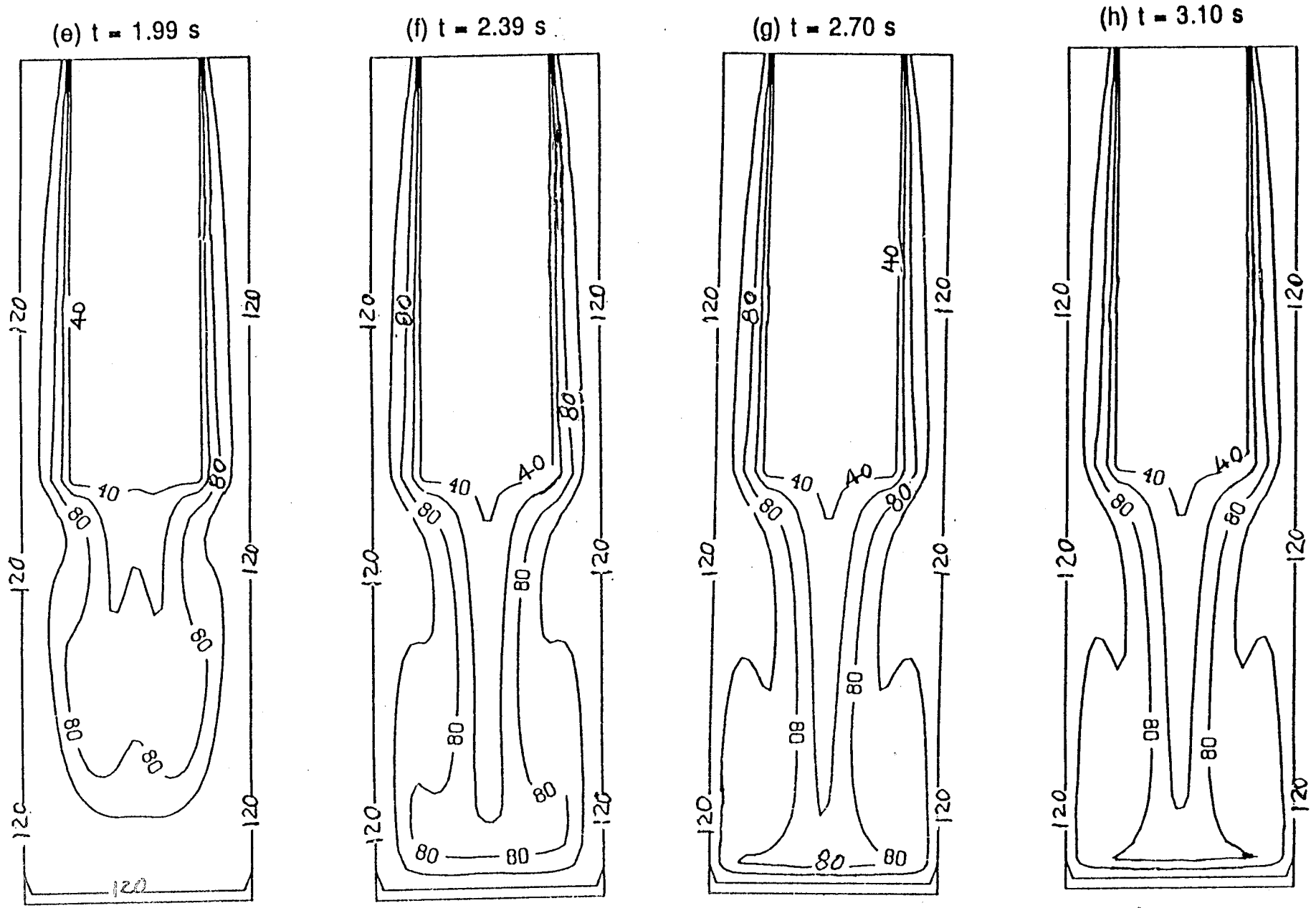

Fig. 5 (B)

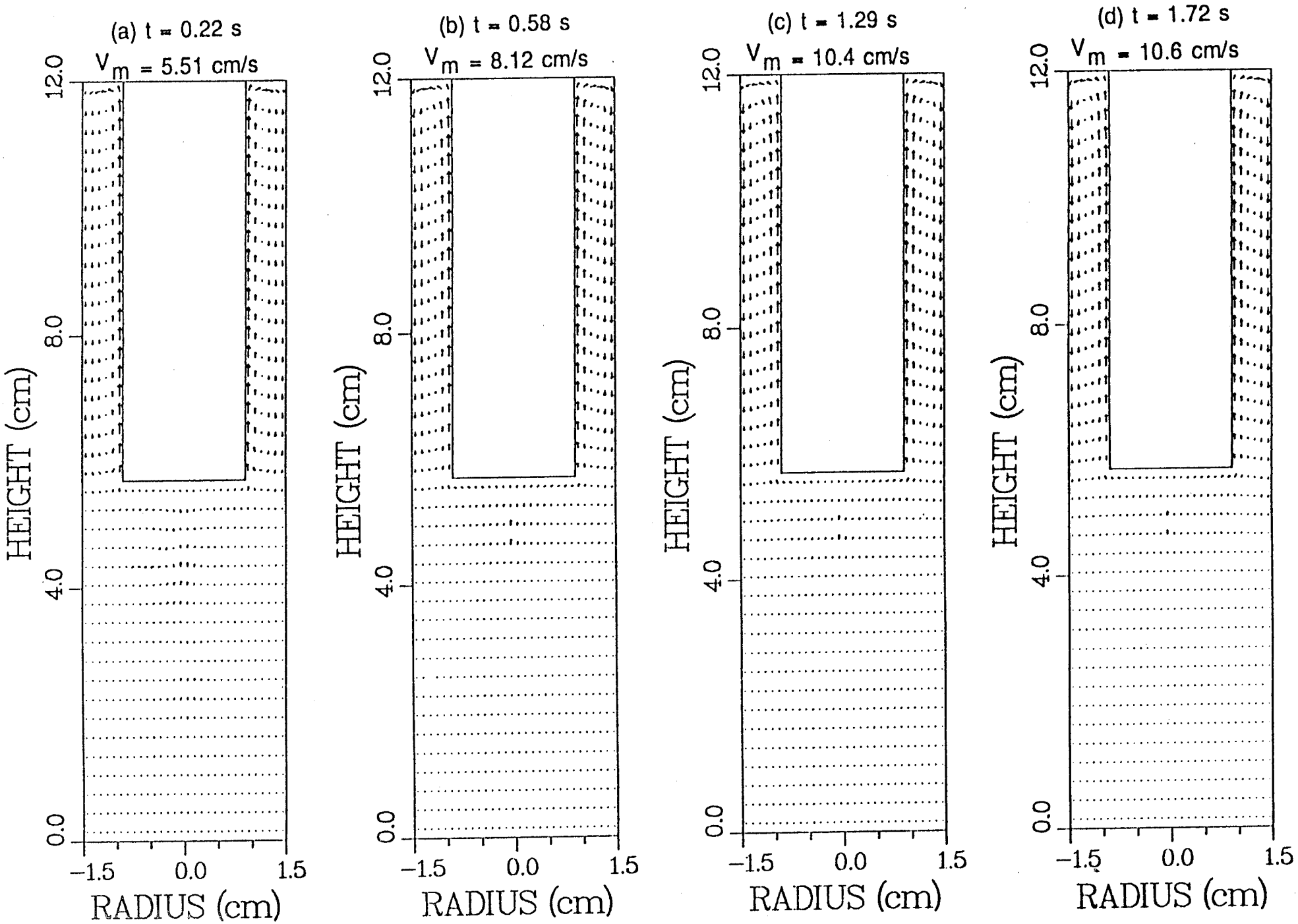
Flow Profile Initiation and Development in r - z Plane at θ = 0° - 180°, ψ = 180°
(a) t = 0.22 s
V_m = 5.51 cm/s
(b) t = 0.58 s
V_m = 8.12 cm/s
(c) t = 1.29 s
V_m = 10.4 cm/s
(d) t = 1.72 s
V_m = 10.6 cm/s
HEIGHT (cm)
0.0
4.0
8.0
12.0
−1.5
0.0
1.5
RADIUS (cm)

Fig. 6 (A)

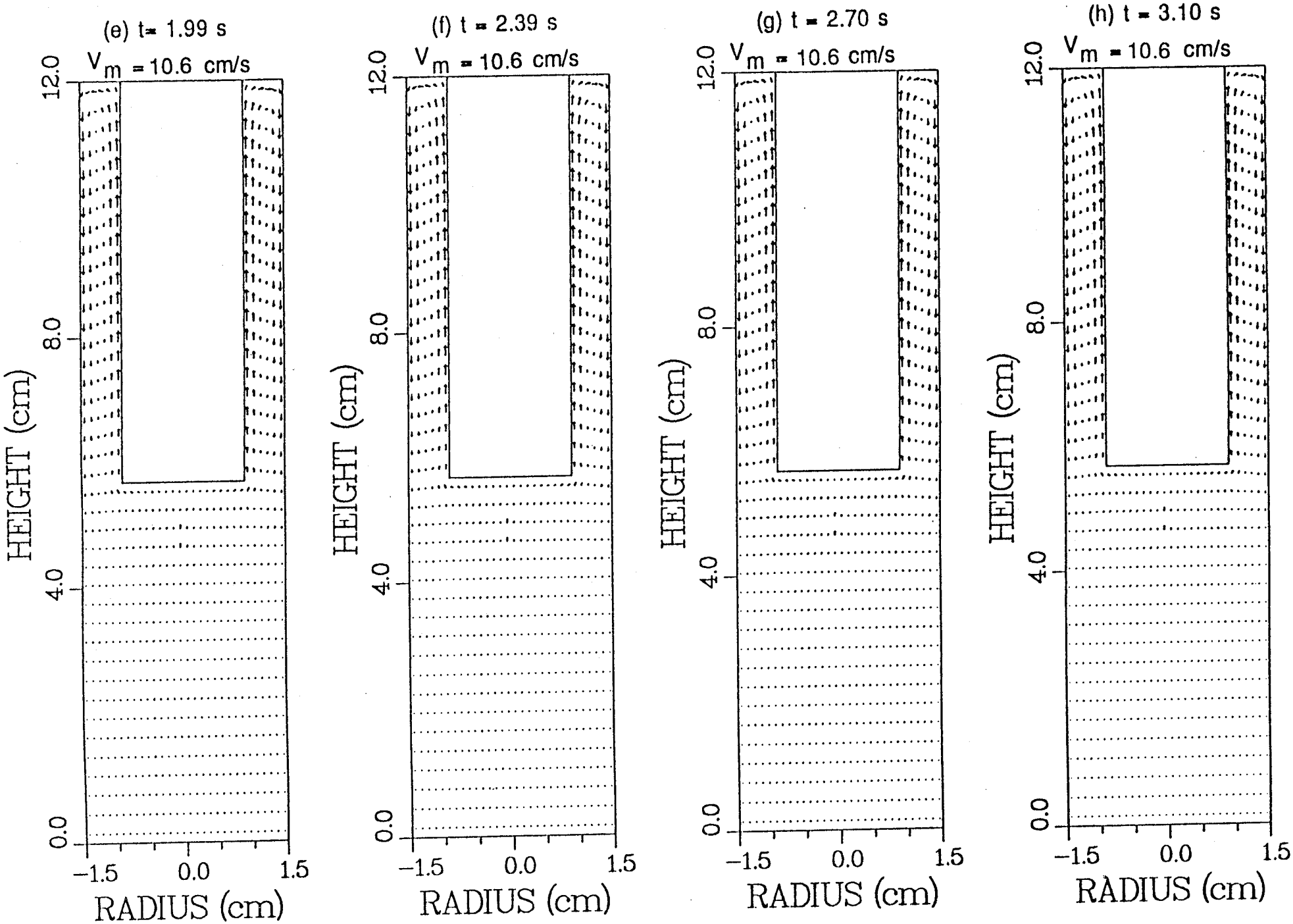
Flow Profile Initiation and Development in r - z Plane at θ = 0° - 180°, ψ = 180°
(e) t= 1.99 s
(f) t = 2.39 s
(g) t = 2.70 s
(h) t = 3.10 s
V_m = 10.6 cm/s
HEIGHT (cm)
RADIUS (cm)
0.0
4.0
8.0
12.0
-1.5
0.0
1.5

Fig. 6 (B)

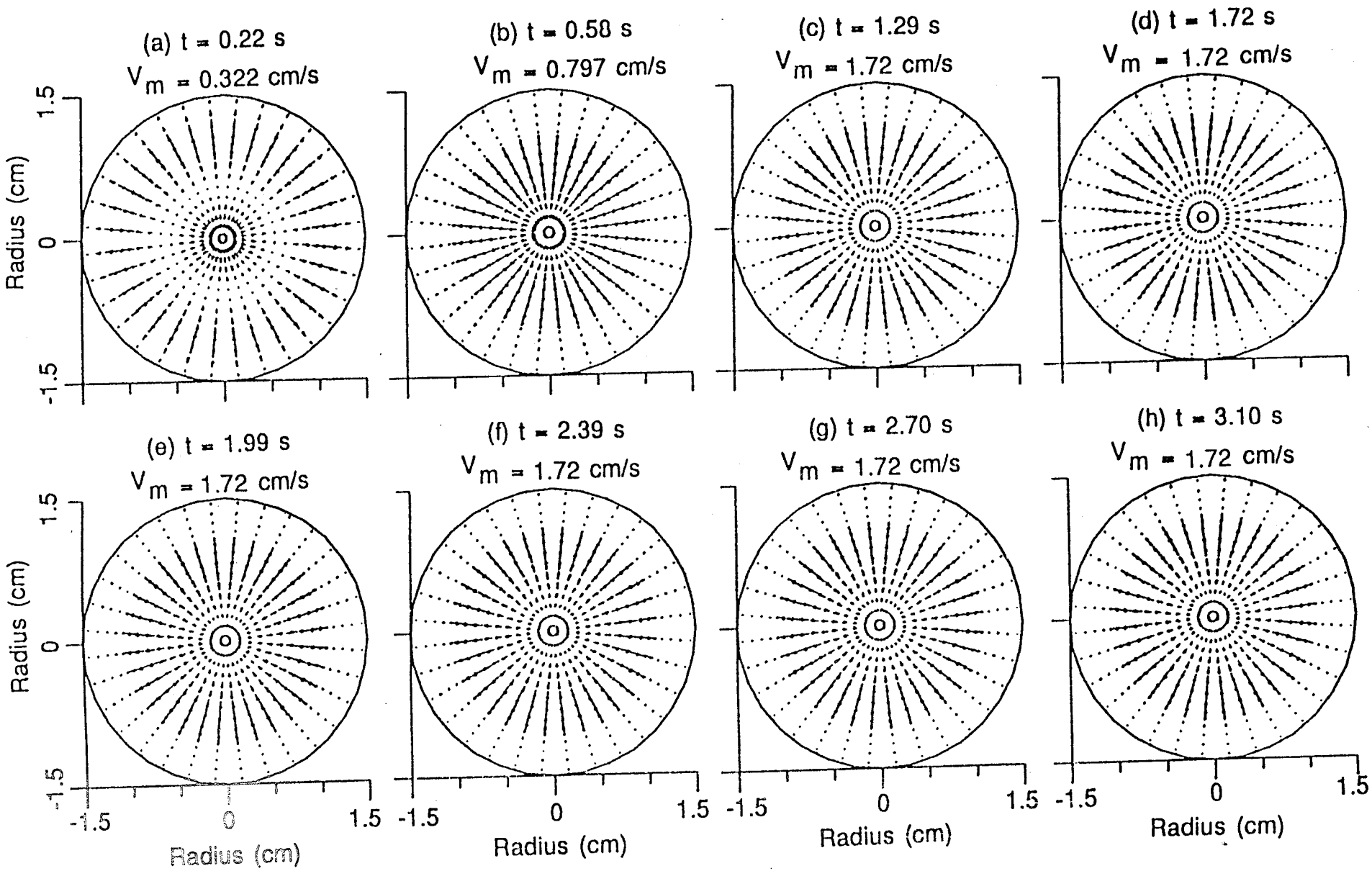
Flow Profile Initiation and Development in r - θ Plane at z = 5.55 cm, ψ = 180°
(a) t = 0.22 s
Vm = 0.322 cm/s
(b) t = 0.58 s
Vm = 0.797 cm/s
(c) t = 1.29 s
Vm = 1.72 cm/s
(d) t = 1.72 s
Vm = 1.72 cm/s
(e) t = 1.99 s
Vm = 1.72 cm/s
(f) t = 2.39 s
Vm = 1.72 cm/s
(g) t = 2.70 s
Vm = 1.72 cm/s
(h) t = 3.10 s
Vm = 1.72 cm/s
Radius (cm)
1.5
0
-1.5
Radius (cm)

Fig. 7

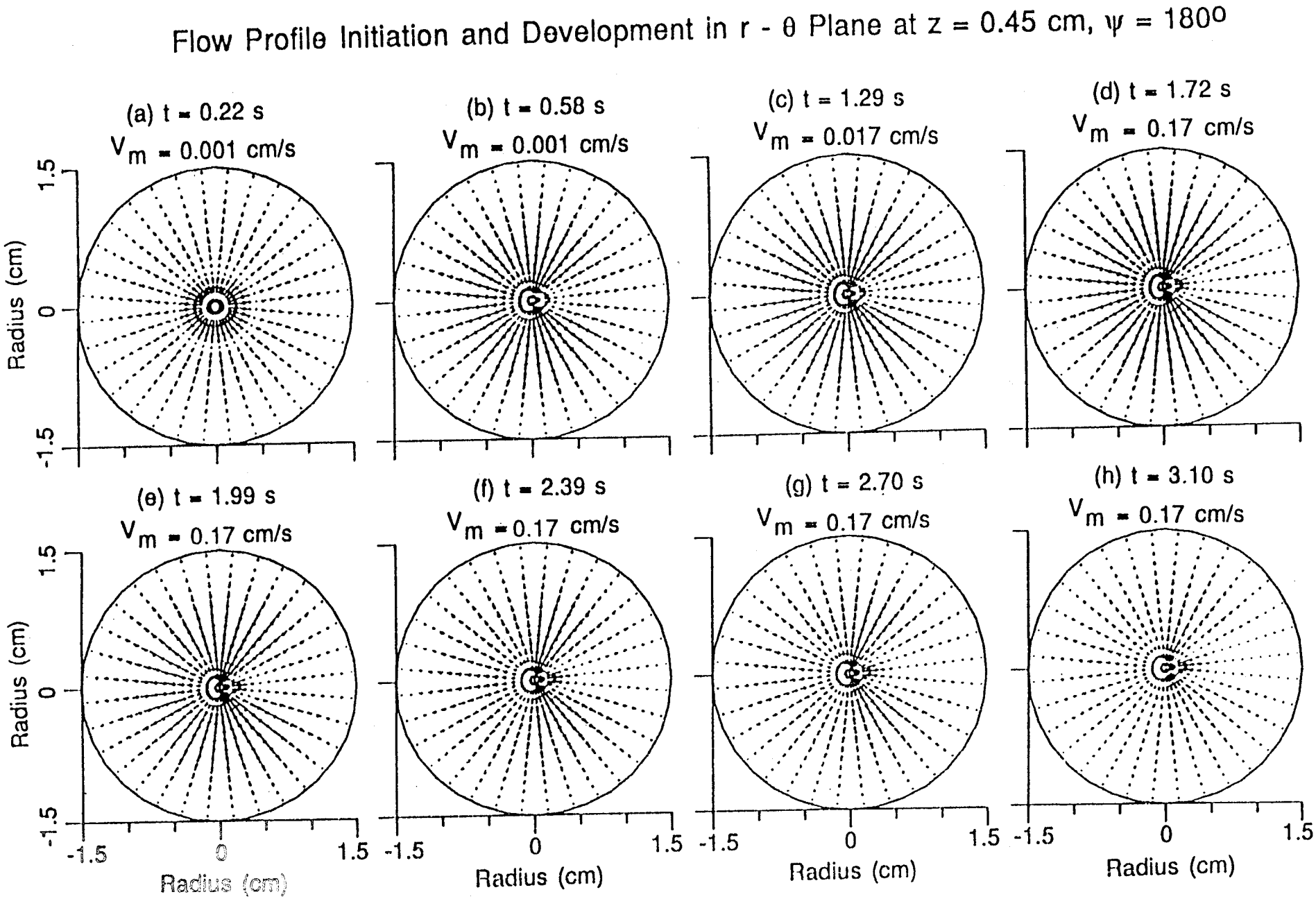
Flow Profile Initiation and Development in r - θ Plane at z = 0.45 cm, ψ = 180°
(a) t = 0.22 s
V_m = 0.001 cm/s
(b) t = 0.58 s
V_m = 0.001 cm/s
(c) t = 1.29 s
V_m = 0.017 cm/s
(d) t = 1.72 s
V_m = 0.17 cm/s
(e) t = 1.99 s
V_m = 0.17 cm/s
(f) t = 2.39 s
V_m = 0.17 cm/s
(g) t = 2.70 s
V_m = 0.17 cm/s
(h) t = 3.10 s
V_m = 0.17 cm/s
Radius (cm)
1.5
0
-1.5
Radius (cm)

Fig. 8

Initiation and Formatiom of Temperature Profile in r - z Plane at $\theta = 0^{o} - 180^{o}$, $\psi = 180^{o}$

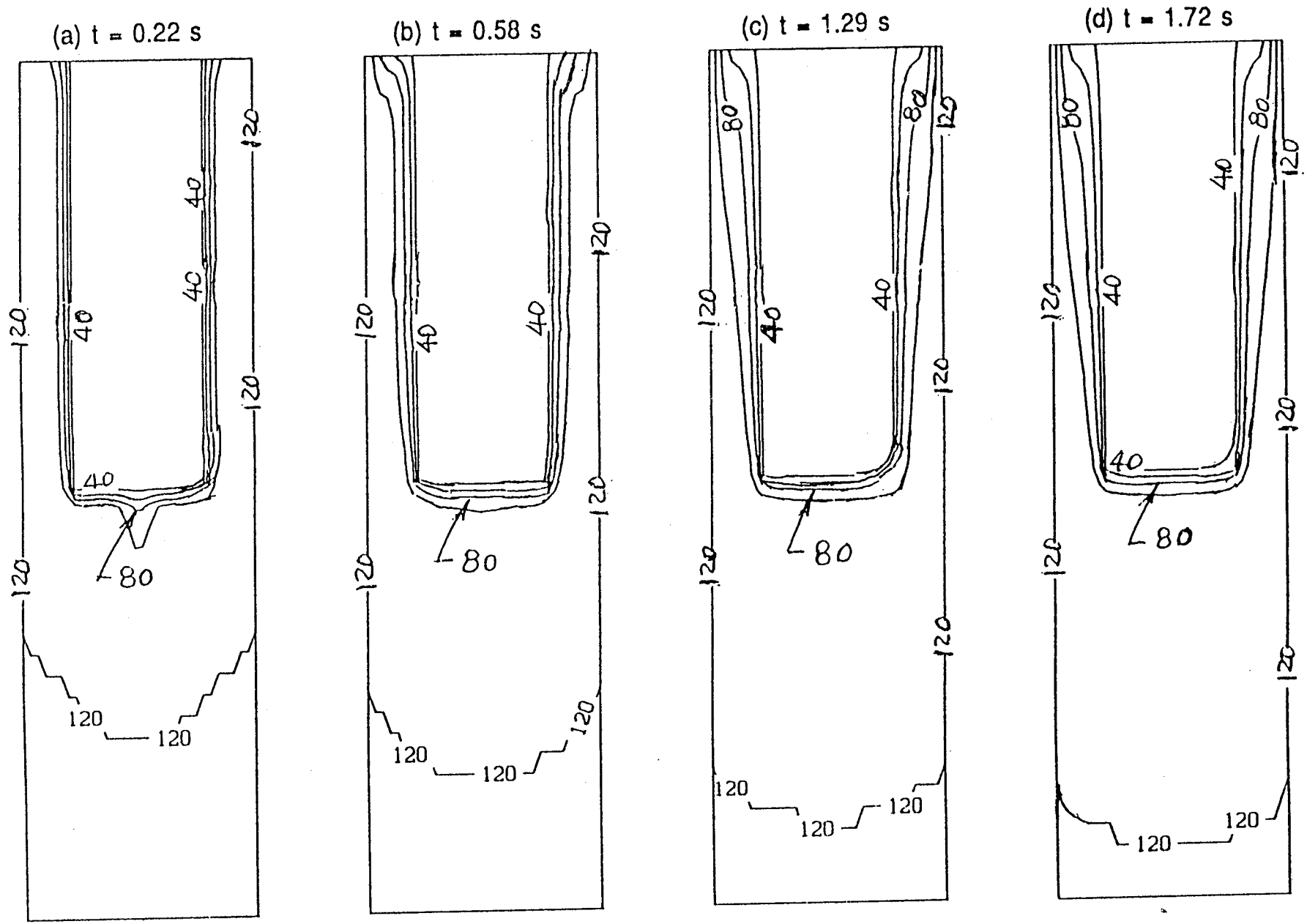

Fig. 9 (A)

Initiation and Formatiom of Temperature Profile in r - z Plane at $\theta = 0^0 - 180^0$, $\psi = 180^0$

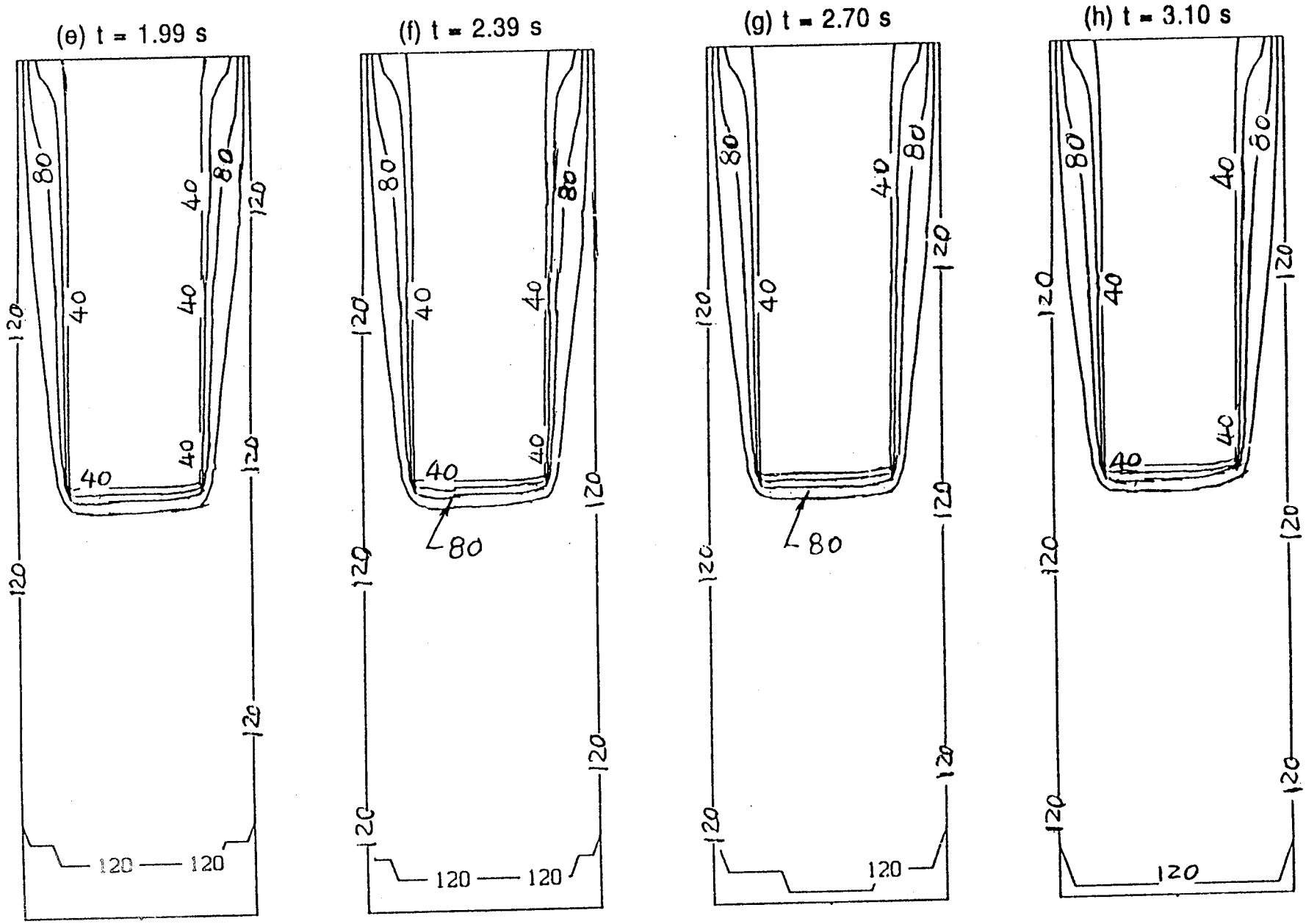

Fig. 9 (B)

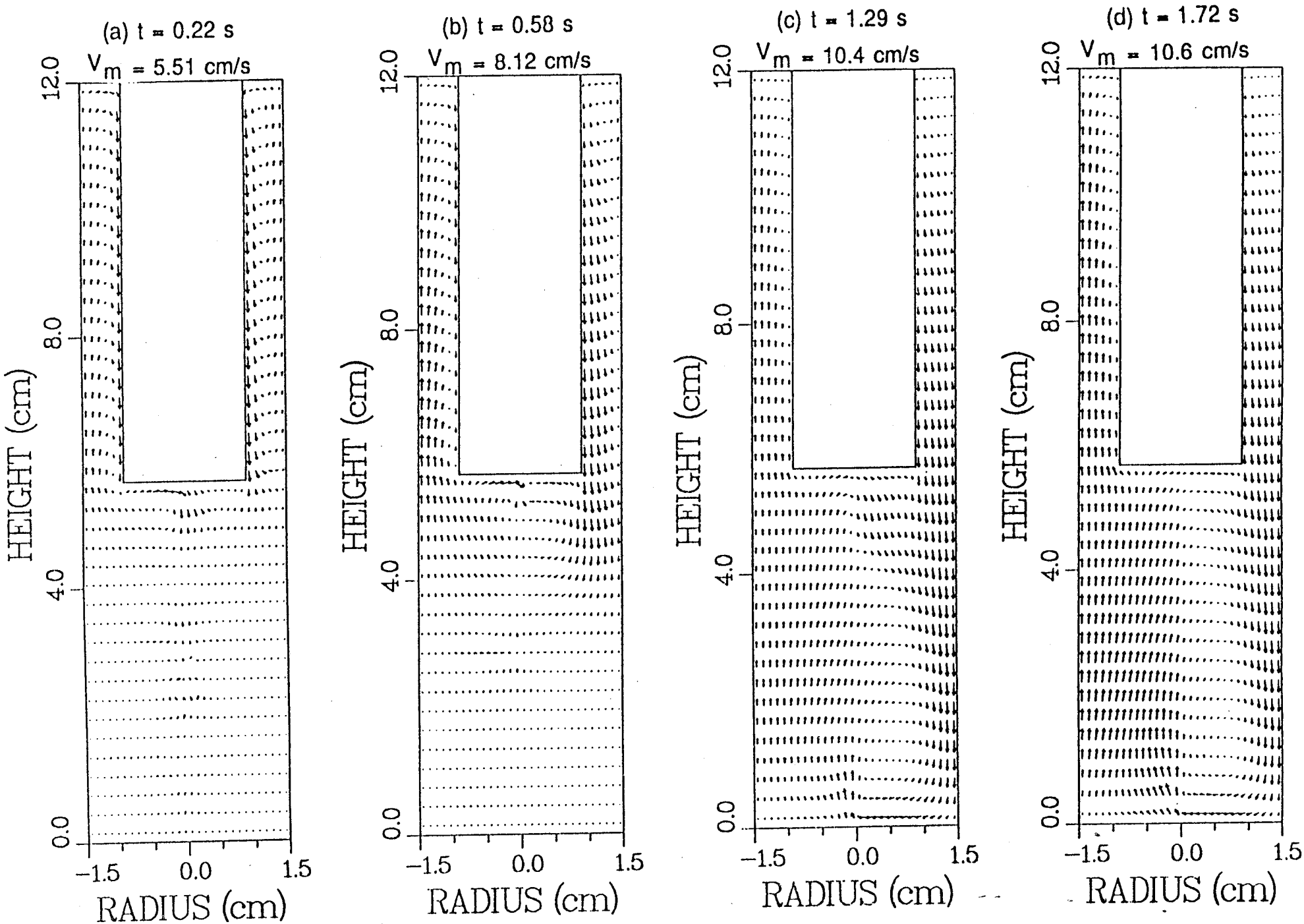
Flow Profile Initiation and Development in r - z Plane at θ = 0° - 180°, ψ = 45°
(a) t = 0.22 s
V_m = 5.51 cm/s
(b) t = 0.58 s
V_m = 8.12 cm/s
(c) t = 1.29 s
V_m = 10.4 cm/s
(d) t = 1.72 s
V_m = 10.6 cm/s
HEIGHT (cm)
12.0
8.0
4.0
0.0
−1.5
0.0
1.5
RADIUS (cm)

Fig. 10 (A)

Flow Profile Initiation and Development in r - z Plane at $\theta = 0^o - 180^o$, $\psi = 45^o$

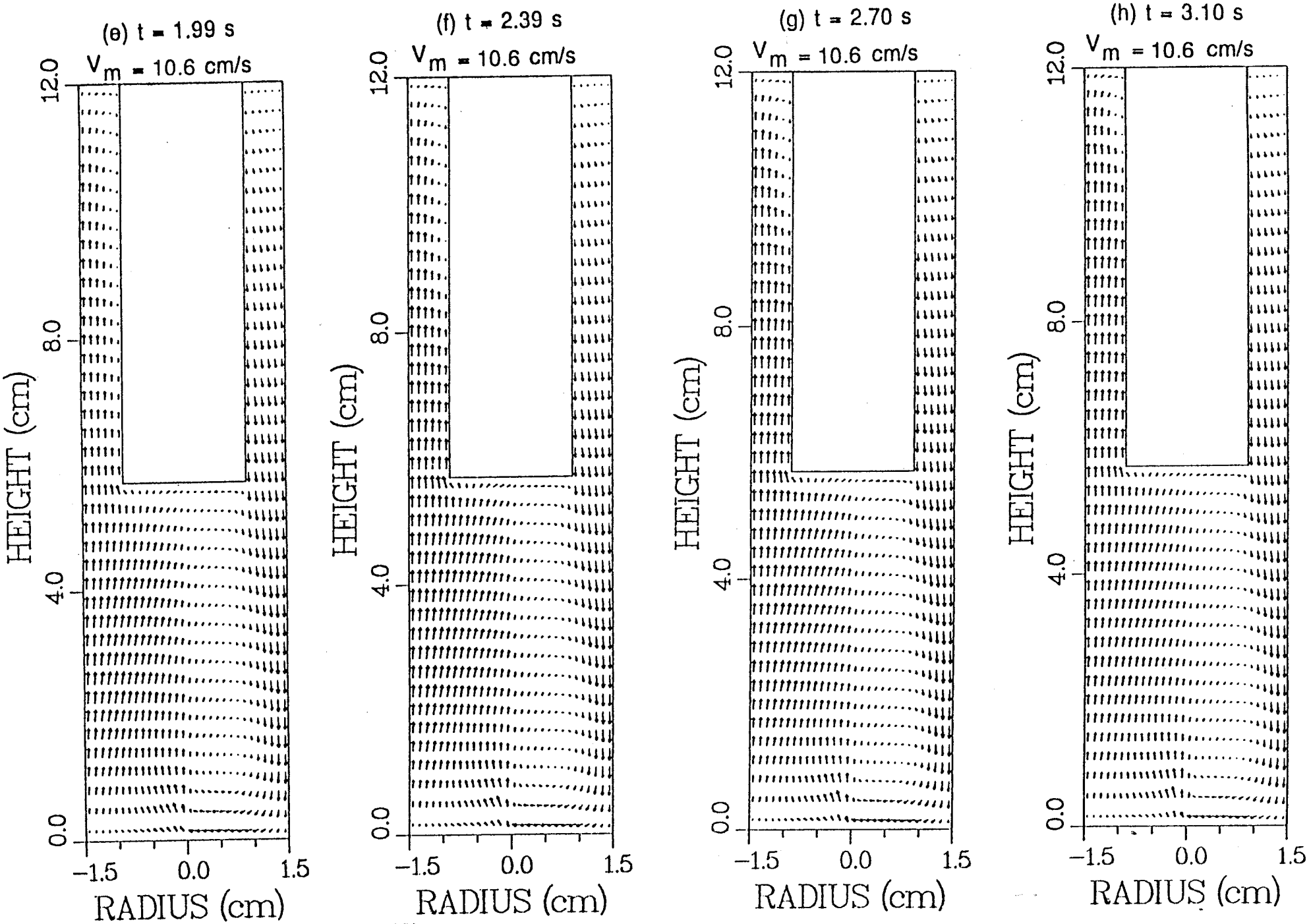

Fig. 10 (B)

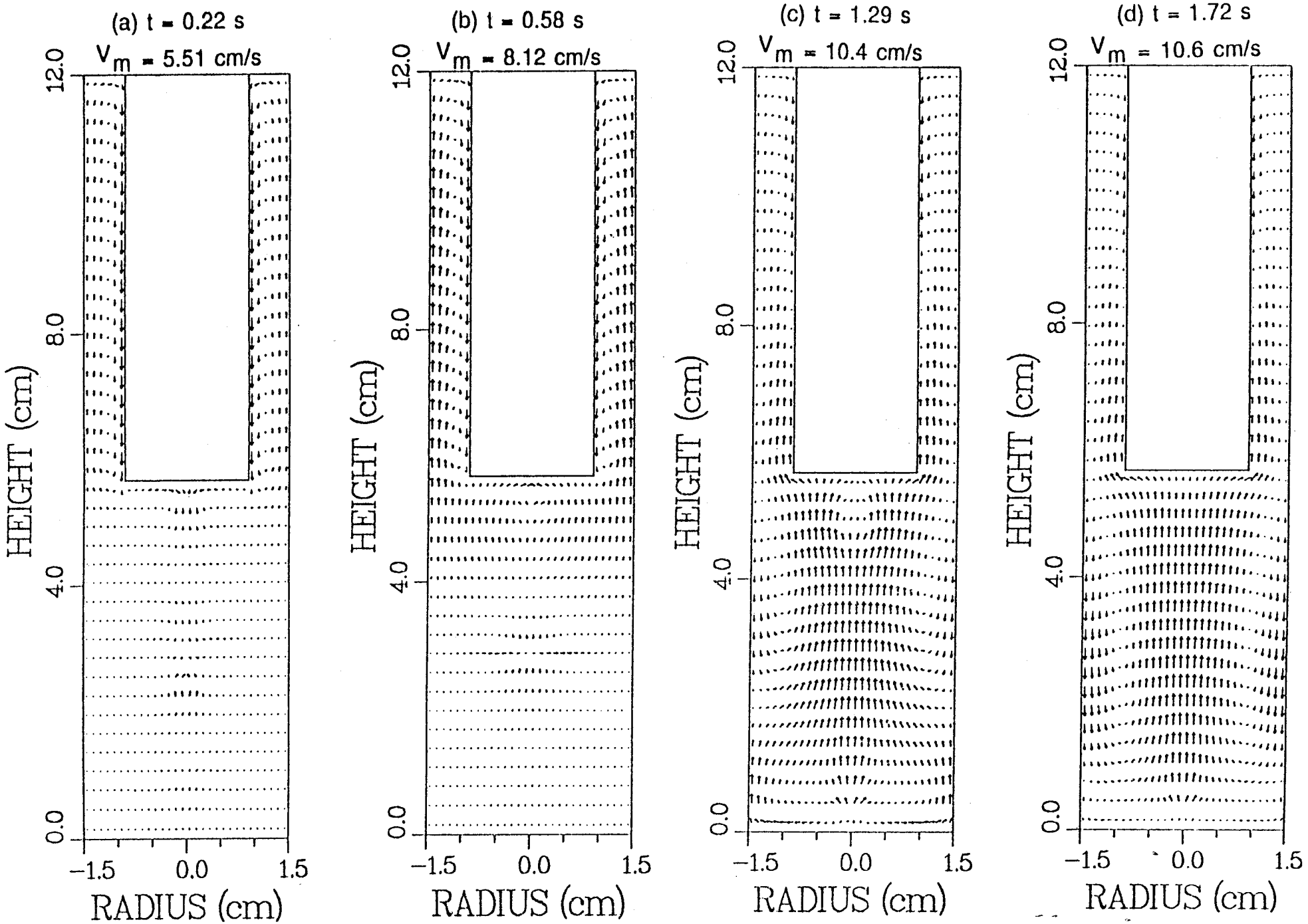
Flow Profile Initiation and Development in r - z Plane at θ = 90° - 270°, ψ = 45°
(a) t = 0.22 s
V_m = 5.51 cm/s
(b) t = 0.58 s
V_m = 8.12 cm/s
(c) t = 1.29 s
V_m = 10.4 cm/s
(d) t = 1.72 s
V_m = 10.6 cm/s
HEIGHT (cm)
12.0
8.0
4.0
0.0
−1.5
0.0
1.5
RADIUS (cm)

Fig. 11 (A)

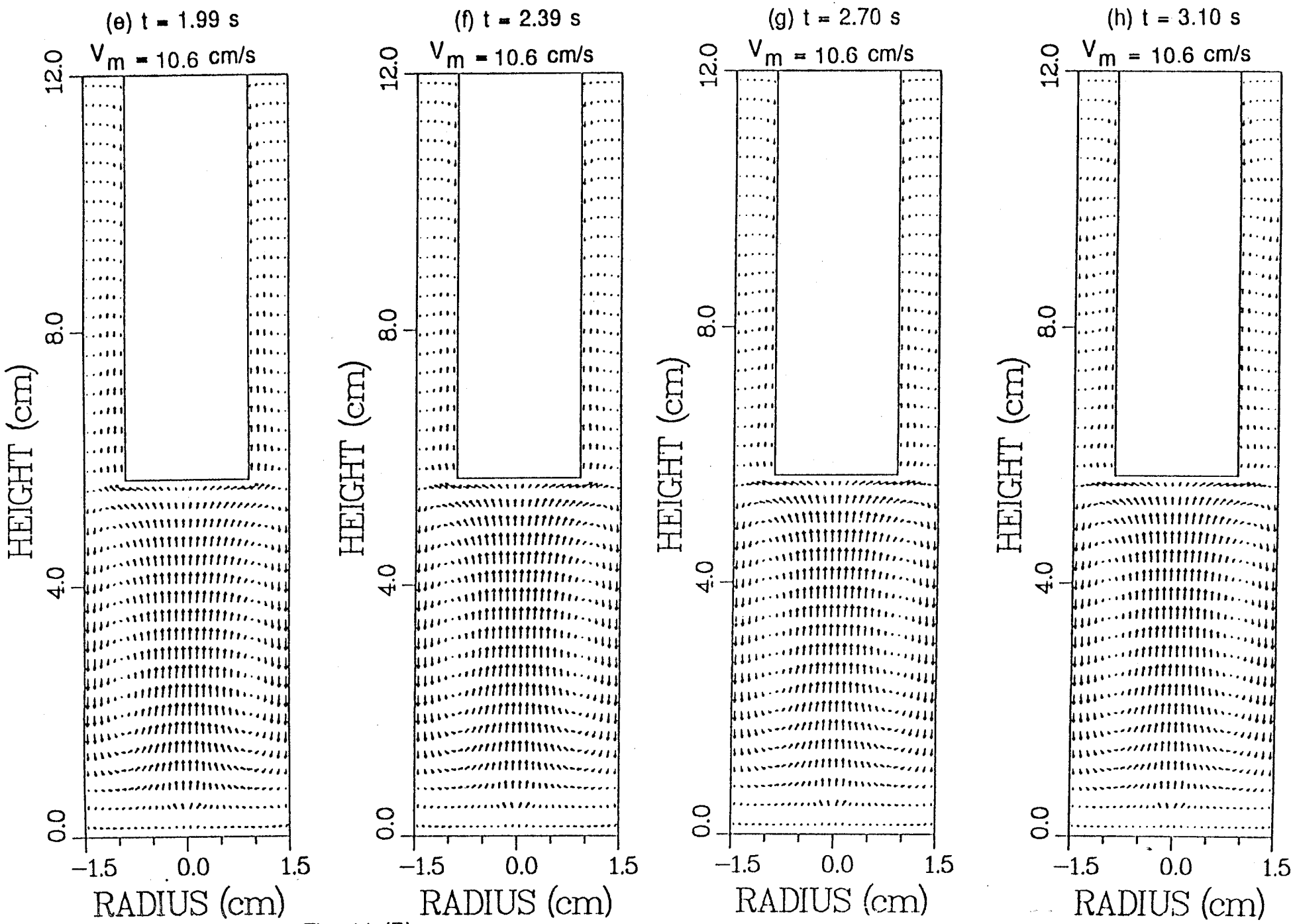
Flow Profile Initiation and Development in r - z Plane at θ = 90° - 270°, ψ = 45°
(e) t = 1.99 s
(f) t = 2.39 s
(g) t = 2.70 s
(h) t = 3.10 s
V_m = 10.6 cm/s
HEIGHT (cm)
RADIUS (cm)
12.0
8.0
4.0
0.0
−1.5
0.0
1.5

Fig. 11 (B)

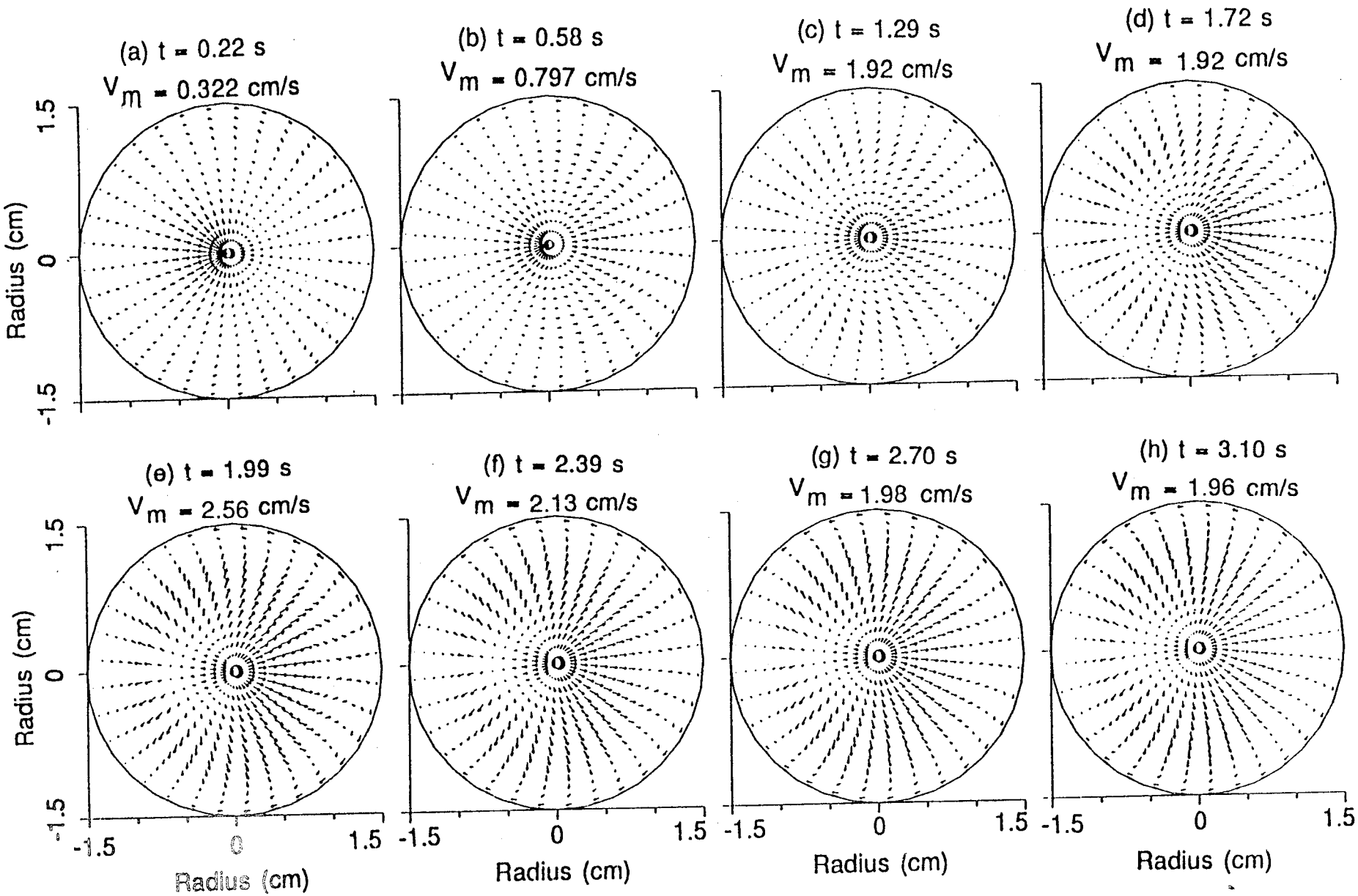
Flow Profile Initiation and Development in r - θ Plane at z = 5.55 cm, ψ = 45°
(a) t = 0.22 s
Vm = 0.322 cm/s
(b) t = 0.58 s
Vm = 0.797 cm/s
(c) t = 1.29 s
Vm = 1.92 cm/s
(d) t = 1.72 s
Vm = 1.92 cm/s
(e) t = 1.99 s
Vm = 2.56 cm/s
(f) t = 2.39 s
Vm = 2.13 cm/s
(g) t = 2.70 s
Vm = 1.98 cm/s
(h) t = 3.10 s
Vm = 1.96 cm/s
Radius (cm)
1.5
0
-1.5
Radius (cm)

Fig. 12

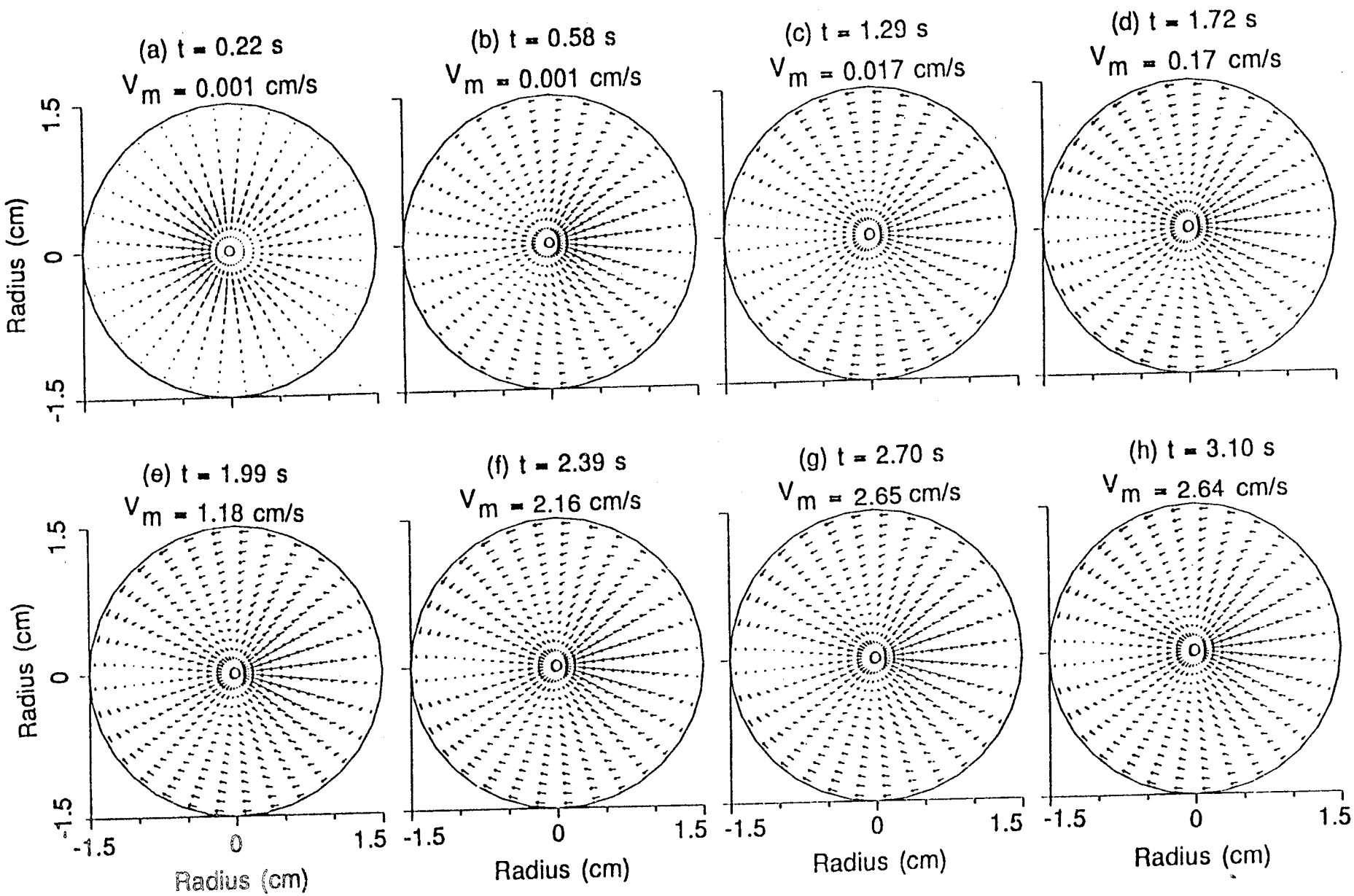
Flow Profile Initiation and Development in r - θ Plane at z = 0.45 cm, ψ = 45°
(a) t = 0.22 s
V_m = 0.001 cm/s
(b) t = 0.58 s
V_m = 0.001 cm/s
(c) t = 1.29 s
V_m = 0.017 cm/s
(d) t = 1.72 s
V_m = 0.17 cm/s
(e) t = 1.99 s
V_m = 1.18 cm/s
(f) t = 2.39 s
V_m = 2.16 cm/s
(g) t = 2.70 s
V_m = 2.65 cm/s
(h) t = 3.10 s
V_m = 2.64 cm/s
Radius (cm)
1.5
0
-1.5
Radius (cm)

Fig. 13

Initiation and Formatiom of Temperature Profile in r - z Plane at θ = 00 - 1800, ψ = 450

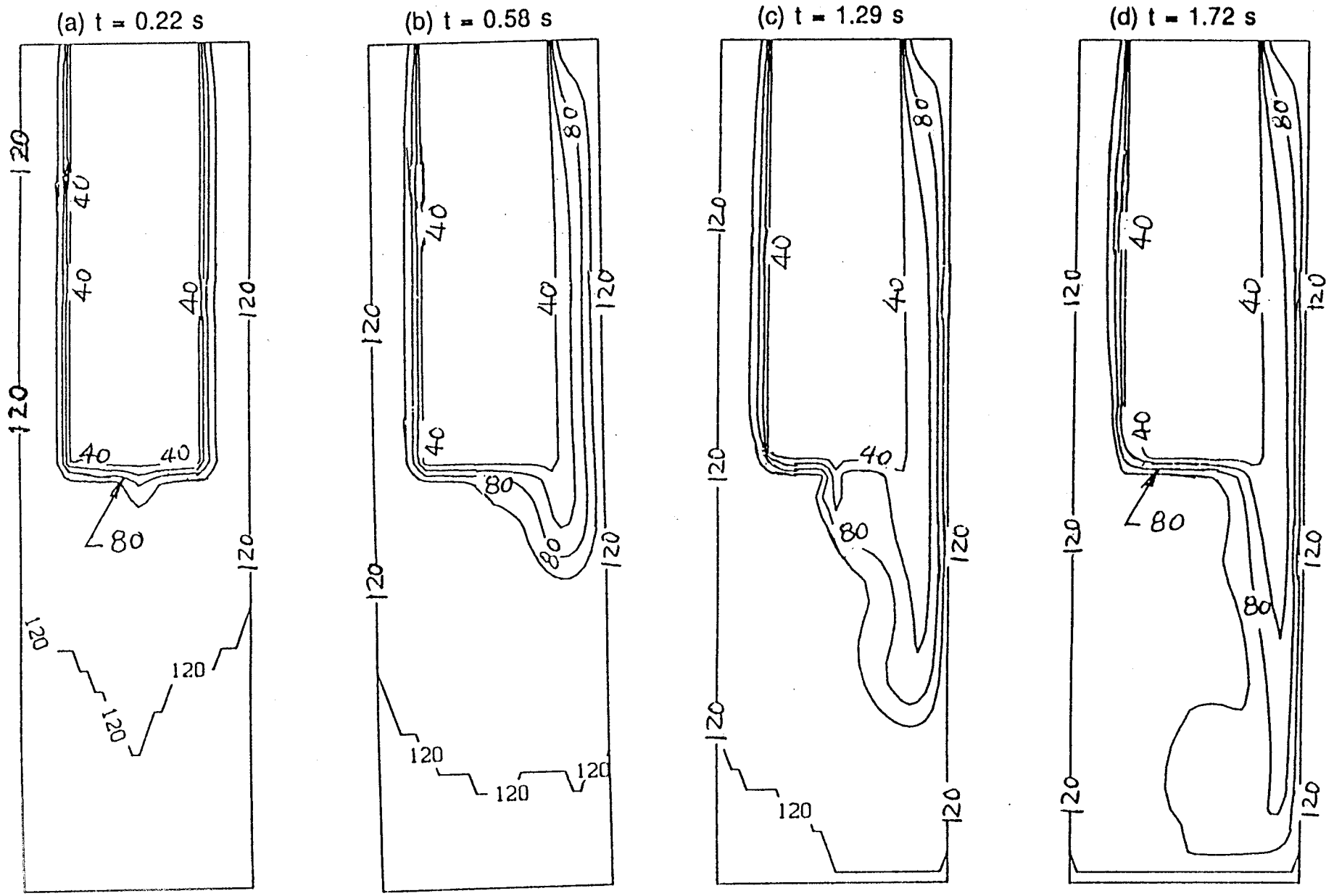

Fig.14(A)

Initiation and Formatiom of Temperature Profile in r - z Plane at $\theta = 0^{o} - 180^{o}$, $\psi = 45^{o}$

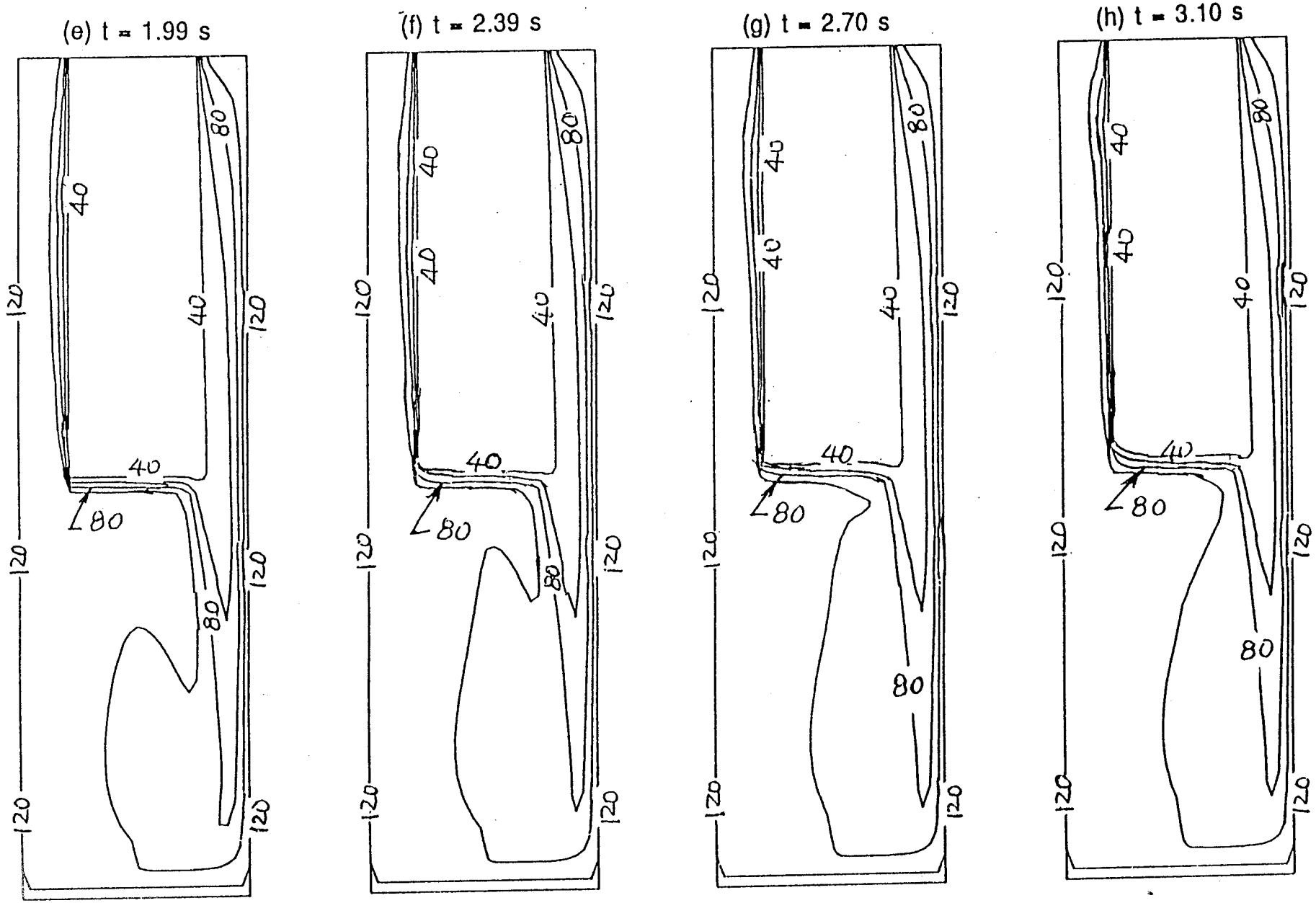

Fig. 14 (B)

Initiation and Formatiom of Temperature Profile in r - z Plane at $\theta = 90^0 - 270^0$, $\psi = 45^0$

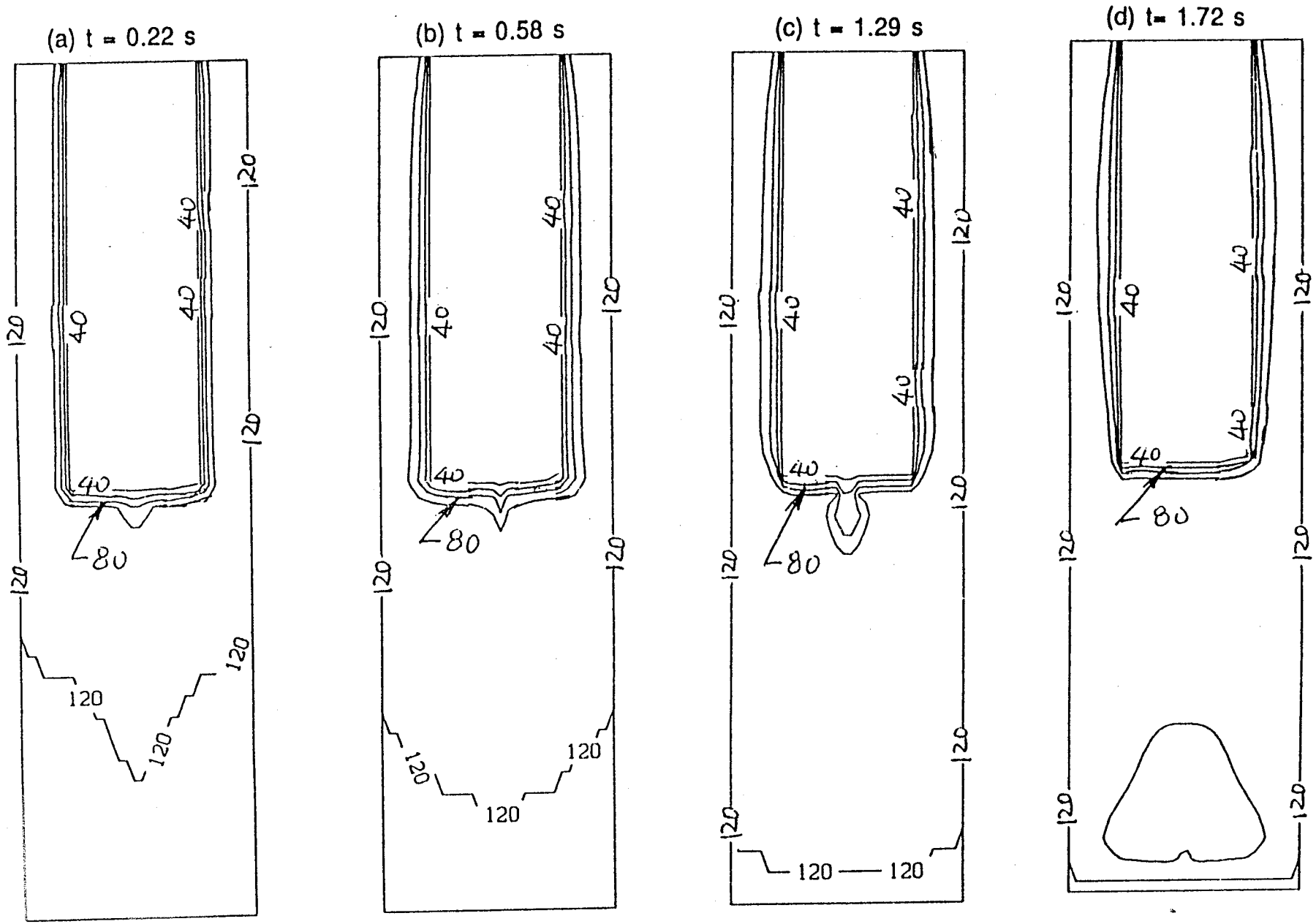

Fig. 15(A)

Initiation and Formatiom of Temperature Profile in r - z Plane at $\theta = 90^{o} - 270^{o}$, $\psi = 45^{o}$

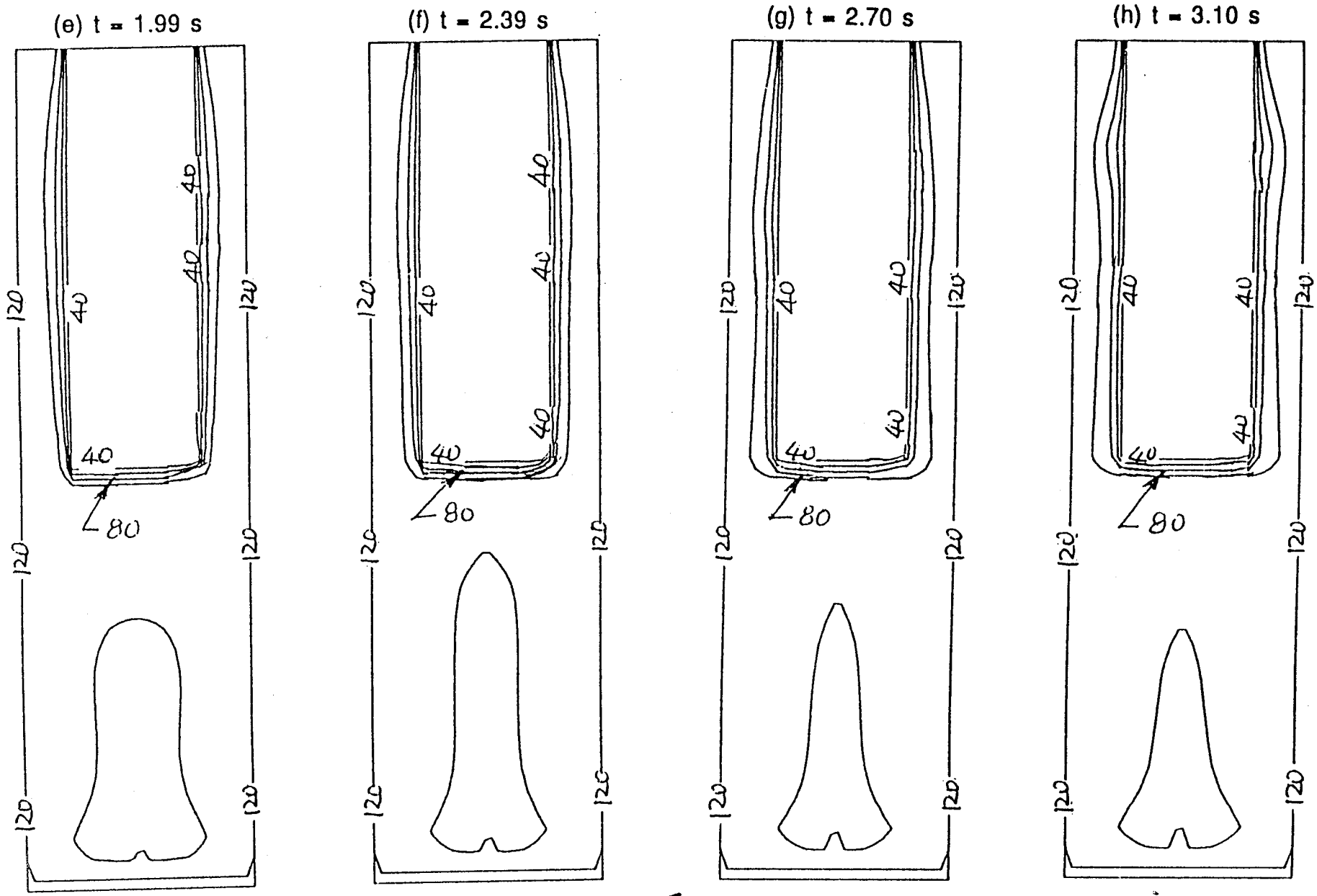

Fig.15 (B)